Volume 4
Number 9
September 2024
Pages 961–1106

Environmental Science
Atmospheres

rsc.li/esatmospheres

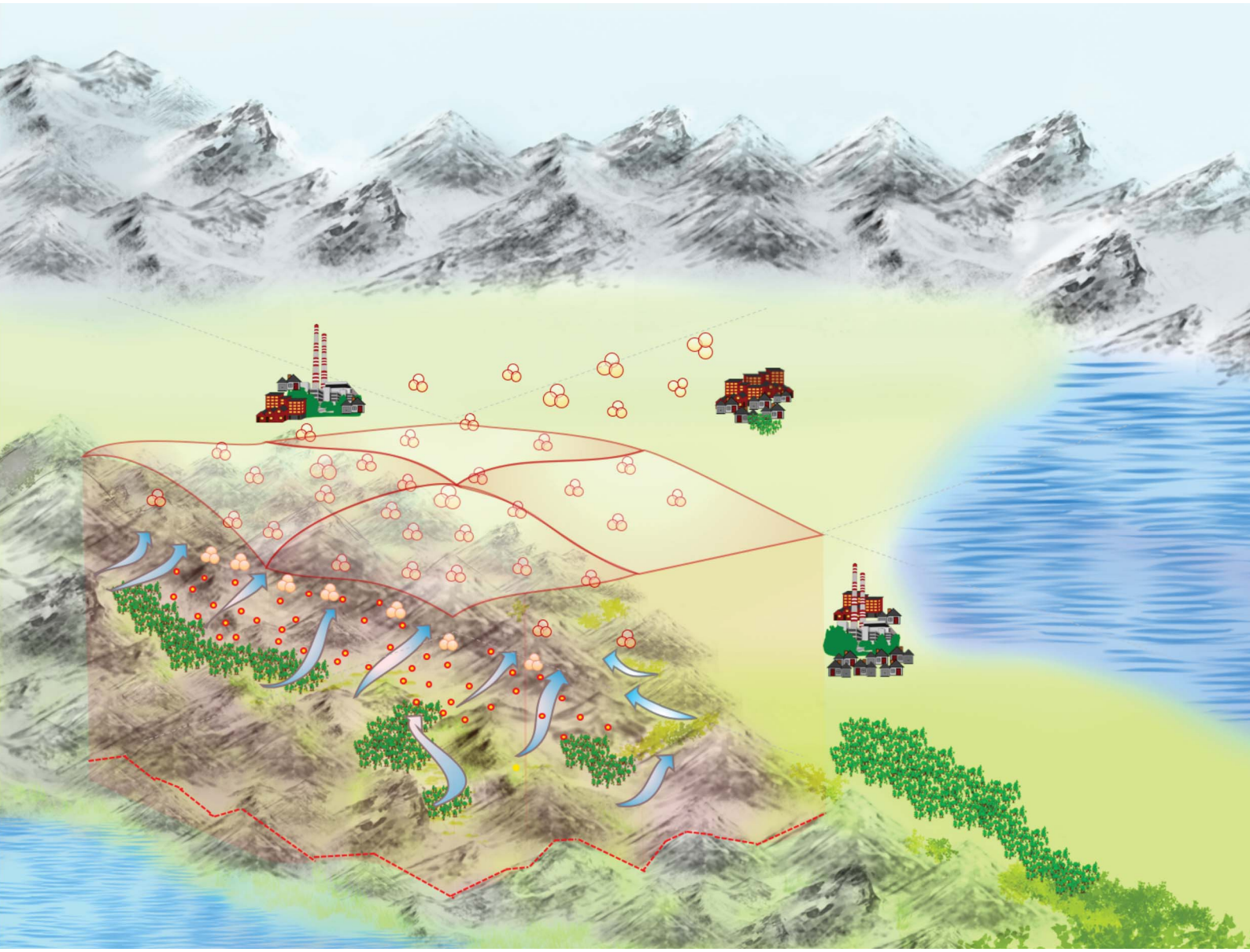

ISSN 2634-3606

ROYAL SOCIETY OF CHEMISTRY

PAPER

Giancarlo Ciarelli *et al.*

Analysis of chemical and transport processes of biogenic aerosols over the northern Apennines: insights from the WRF-CHIMERE model

Environmental Science: Atmospheres

ROYAL SOCIETY OF CHEMISTRY

PAPER

View Article Online
View Journal | View Issue

Cite this: *Environ. Sci.: Atmos.*, 2024, **4**, 967

Analysis of chemical and transport processes of biogenic aerosols over the northern Apennines: insights from the WRF-CHIMERE model†

Bruno Vitali, [abk] Manuel Bettineschi,[b] Arineh Cholakian, [c] Dino Zardi, [ad] Federico Bianchi, [b] Victoria A. Sinclair, [b] Johannes Mikkola,[b] Paolo Cristofanelli, [e] Angela Marinoni,[e] Martina Mazzini,[e] Liine Heikkinen,[f] Minna Aurela, [g] Marco Paglione, [e] Bertrand Bessagnet,[ch] Paolo Tuccella[ij] and Giancarlo Ciarelli *[b]

Sources and transport processes of aerosols over the Italian northern Apennines are investigated with a focus on the area of the WMO/GAW global station of Mt. Cimone (CMN, 2165 m a.s.l.). The site is characterized by complex orography, representing a challenge for chemical transport model (CTM) applications when simulating processes controlling advection and diffusion of air pollutants within and above the planetary boundary layer (PBL). First, we extensively evaluated the skills of the WRF-CHIMERE (v2020r3) coupled CTM in reproducing both the meteorological conditions observed at the surface level of multiple weather stations and the sub-micrometre aerosol mass concentrations from intensive *in situ* measurements performed at CMN during July 2017. The analysis of the meteorological fields revealed that the local thermally-driven flows occurring over the adjacent coastal and mountainous regions are very well reproduced by the model. The accuracy is less at higher altitudes in proximity of CMN and on the slopes facing the Po valley, where also fewer observational meteorological data were available. The discrepancies between the model output and observations, especially in the near-surface wind dynamics, are mainly associated with the smoothed topography of the terrain as represented in the model: at the resolution of 1 km small-scale orographic features and related meteorological phenomena cannot be adequately reproduced. Our results indicate that the modeled particle mass concentrations and its chemical composition are in good agreement with observational data, with organic aerosol contributing to about 60% of the total sub-micrometer aerosol load during the investigated time period and sulphate being the most important inorganic component. Additionally, a model-based source apportionment analysis revealed that organic aerosol, and specifically secondary organic aerosol (SOA), were mostly of biogenic origin (contributing up to 66% of the secondary organic aerosol fraction). We further analyze the transport of organic aerosol particles associated with the typical wind pattern developing at the interface between plains, valleys and ridges of the northern Apennines mountains. Despite uncertainties in source areas and formation mechanisms, the model results indicated that the upslope valley winds might sustain the funneling of biogenic aerosol particles to higher elevations up to the Apennines ridge, eventually to above the diagnosed PBL height. For biogenic organic aerosol this process is more effective on the south-western slope of the Apennines range. This may result from

Received 29th March 2024
Accepted 3rd July 2024

DOI: 10.1039/d4ea00040d

rsc.li/esatmospheres

[a]*Department of Civil, Environmental and Mechanical Engineering, University of Trento, Trento, Italy*

[b]*Institute for Atmospheric and Earth System Research/Physics, Faculty of Science, University of Helsinki, Helsinki, 00014, Finland. E-mail: giancarlo.ciarelli@helsinki.fi*

[c]*Laboratoire de Météorologie Dynamique (LMD), IPSL, École Polytechnique, Institut Polytechnique de Paris, ENS, PSL Research University, Sorbonne Université, CNRS, Palaiseau, France*

[d]*Center Agriculture Food Environment – C3A, University of Trento, Trento, Italy*

[e]*Institute of Atmospheric Sciences and Climate, National Research Council of Italy (ISAC-CNR), 40129 Bologna, Italy*

[f]*Department of Environmental Science and Bolin Centre for Climate Research, Stockholm University, Stockholm, Sweden*

[g]*Finnish Meteorological Institute, Erik Palménin aukio 1, 00560 Helsinki, Finland*

[h]*European Commission, Joint Research Centre (JRC), 21027 Ispra, Italy*

[i]*Department of Physical and Chemical Sciences, University of L'Aquila, L'Aquila, Italy*

[j]*Center of Excellence in Telesensing of Environment and Model Prediction of Severe Events (CETEMPS), University of L'Aquila, 67100 L'Aquila, Italy*

[k]*Sustainable Development and Energy Sources, Ricerca sul Sistema Energetico SpA, Milan, Italy*

† Electronic supplementary information (ESI) available. See DOI: https://doi.org/10.1039/d4ea00040d

either more favourable meteorological conditions or larger availability of aerosol particles over the lowlands. This work represents the first high-resolution (1 km) CTM study investigating the region of Mt. Cimone and is intended to provide original insights on the vertical transport of aerosols particles into the free troposphere in regions characterized by a complex orography, such as the Alpine range, the European Alps, and the Apennines.

Environmental significance

About 30% of the Earth's land surface is covered with mountains. These regions are the home of a large fraction of the global biodiversity, including a multitude of plant species, which are often crucial for the survival of the nearby human settlements. The Apennines range, specifically, extends for about 1200 kilometers along the Italian peninsula, providing a reservoir of biogenic volatile organic compounds that can be converted into aerosol particles and transported by the typical wind pattern occurring in mountain valleys. Our studies aim at characterizing such processes by means of high-resolution model simulations in order to improve the understanding of the final climate impacts of such mechanisms.

1 Introduction

Determining the fate of atmospheric pollutants is much more complicated over mountains than over flat terrain. Indeed, a variety of airflows develop over mountains, driven either by synoptic- or meso-scale systems interacting with topographic barriers, *i.e.* dynamically-driven flows,[1] or promoted by the daily-periodic cycle of surface heating and cooling, *i.e.* thermally-driven flows.[2] The former type typically allows for longer trajectories (such as those associated with mountain waves), while the latter may lead to either stronger mixing during daytime convective situations, or stagnation in cold pools during stable situations.[3] In particular, mountain valleys, where many sources of both anthropogenic and biogenic pollutants concentrate, are known to promote both daily periodic along-valley winds, and combined cross-valley circulations. These are associated with either up- or down-slope winds over the valley sidewalls, which control the development of boundary layer structures.[4] The complexity of the above-mentioned circulation patterns, and of the associated atmospheric boundary layer processes over mountainous regions, have been extensively treated in Steyn *et al.*[5] and more recently updated in a series of coordinated contributions (see Zardi *et al.*[6] for an overview). In particular, challenges for air pollution monitoring and modelling arising from mountain processes have been thoroughly reviewed in Giovannini *et al.*[7]

Past studies applying state-of-the-art mesoscale models over Alpine valleys have shown that the representation of the main features of typical mountain circulations, such as valley winds, greatly benefits from horizontal resolutions as small as about 1 km.[8] The increased model ability in simulating thermally-driven winds can be attributed to a more accurate representation of the topography, rather than to a more explicit modelling of turbulent processes, in particular in case of medium to large valleys.[9] For example, Mikkola *et al.*[10] recently simulated valley winds in four steep valleys in the Nepal Himalayas with a ~1 km horizontal grid-spacing, finding good agreement between simulated and observed diurnal cycles of near-surface variables. However, over smaller-scale mountainous landforms, a more accurate modelling of the PBL scale, primarily impacting on pollutant diffusion, requires higher resolutions, with horizontal gridsteps down to few hundred metres, and a careful application of turbulence closure schemes specifically developed for the so-called "grey-zone", *i.e.* the scale where atmospheric processes are not fully resolvable.[7] Moreover, high-resolution CTM applications over complex terrain remain challenging due to the substantial computational load compared to typical regional applications, with a resolution of about 20–30 km.

A large number of modelling studies focused on the transport of both primary and secondary pollutants in the Po Valley *e.g.*[11–15] However, only a few CTM applications investigated the interactions of air pollutants with the surrounding mountains, *i.e.* the Italian Alps and the Apennines. Among the few examples, the recent project B-TEX[16] explored the fate of pollutants emitted by a continuous pointwise elevated source in the basin surrounding the city of Bolzano (Italian Alps). The experiment included a series of atmospheric measurements, combining surface stations and ground-based remote sensing devices. Also, tracer experiments were performed under different stability conditions.[17] Measurements showed how complex interactions of surface-layer processes and valley wind systems occur therein.[18,19] Such complex situations required a careful calibration of surface schemes[20] in view of deriving satisfactory results from numerical modelling of atmospheric processes at the required high resolution. The goal of reproducing the observed pollutant concentrations by means of suitable dispersion models required testing different approaches (including both Eulerian and Lagrangian schemes), and a variety of closures for the parameterisation of turbulence mixing.[21]

In another study, Diémoz *et al.*[22] investigated the transport of aerosol pollutants to the northwestern Alps by combining both Lagrangian (LAGRANTO) and Eulerian (FARM, Flexible Air quality Regional Model) modeling tools down to 1 km resolution. They found that aerosol particles can be advected upvalley and effectively produce high particulate matter concentrations in the Aosta valley (summer case study), with detrimental effects on the air quality of the investigated Alpine region. While the arrival of aerosol pollutants was correctly attributed to sources external to the valley, the model underestimated the total PM_{10} (*i.e.*, aerosol particles with an aerodynamic diameter less than 10 μm) mass and predicted the daily maximum 6–7 hours before it was observed. The authors concluded that uncertainties in the emission inventories are likely the cause for such underestimation, whereas timing error in the daily PM_{10}

concentration maxima are likely related to uncertainties in the meteorological model (COSMO, Consortium for Small-scale Modeling, http://www.cosmo-model.org) in reproducing the up-valley and down-valley winds.

The recent increasing availability of data from meteorological and air composition measurements, either from continuous monitoring programmes or from targeted field campaigns at high-altitude sites, offers the unprecedented opportunity to evaluate both meteorological and pollutant transport models in complex terrain areas. Examples of such stations are the Jungfraujoch (3580 m above sea level – a.s.l.) in the Western Swiss Alps, and the Puy-de-Dome (1465 m a.s.l.) in central France.[23,24] In Italy, the WMO/GAW global station of Mt. Cimone (2165 m a.s.l.) represents a state-of-the-art high-altitude research station for the study of background atmospheric conditions. It is located in the northern Apennines, adjacent to the highly-polluted Po plain and nearly at the centre of the Mediterranean basin.[25] Among various intensive field campaigns based at Mt. Cimone (hereafter referred to as CMN), the Aerosol, Clouds and Trace Gases Research Infrastructure (ACTRIS-2) campaign took place in summer 2017. The campaign was focused on the absorbing aerosol closure, but the large dataset collected simultaneously over multiple measurement sites in the Po Valley allows assessing the accuracy of model simulations over high and complex terrain and studying the transport of air masses over the Po river basin and at a regional scale. However, so far very few CTM applications focusing on this location are available (*e.g.*, Brattich *et al.*[26]).

In this study, we used the WRF-CHIMERE v2020r3 model[27] in a high-resolution configuration with 4 nested domains centered over the northern Apennines during July 2017 in order to (i) evaluate the model's ability to correctly simulate meteorological variables and the aerosol mass and chemical composition in complex terrain, and (ii) to investigate aerosols' chemical and regional sources at the station of CMN. Specifically, this study aims at quantifying the transport of biogenic particles from valley floors of the Apennines valleys to higher elevations.

The manuscript is organized as follows: Section 2 briefly presents the area of CMN and its topographic characteristics. Section 3 describes the observational data, their spatial distribution and the WRF-CHIMERE v2020r3 model setup for the study. In Section 4 the results of the meteorological and aerosol model evaluation are presented, while Section 5 reports the analysis of the aerosol transport patterns and source apportionment of PM_1. In Section 6 section we report the summary and the main conclusions of the study.

2 Geographical framework: the northern Apennines

The Mt. Cimone GAW/WMO Global Station ('CMN',44°11′N, 10° 42′E, 2165 m a.s.l.) is located on the highest peak of the Italian

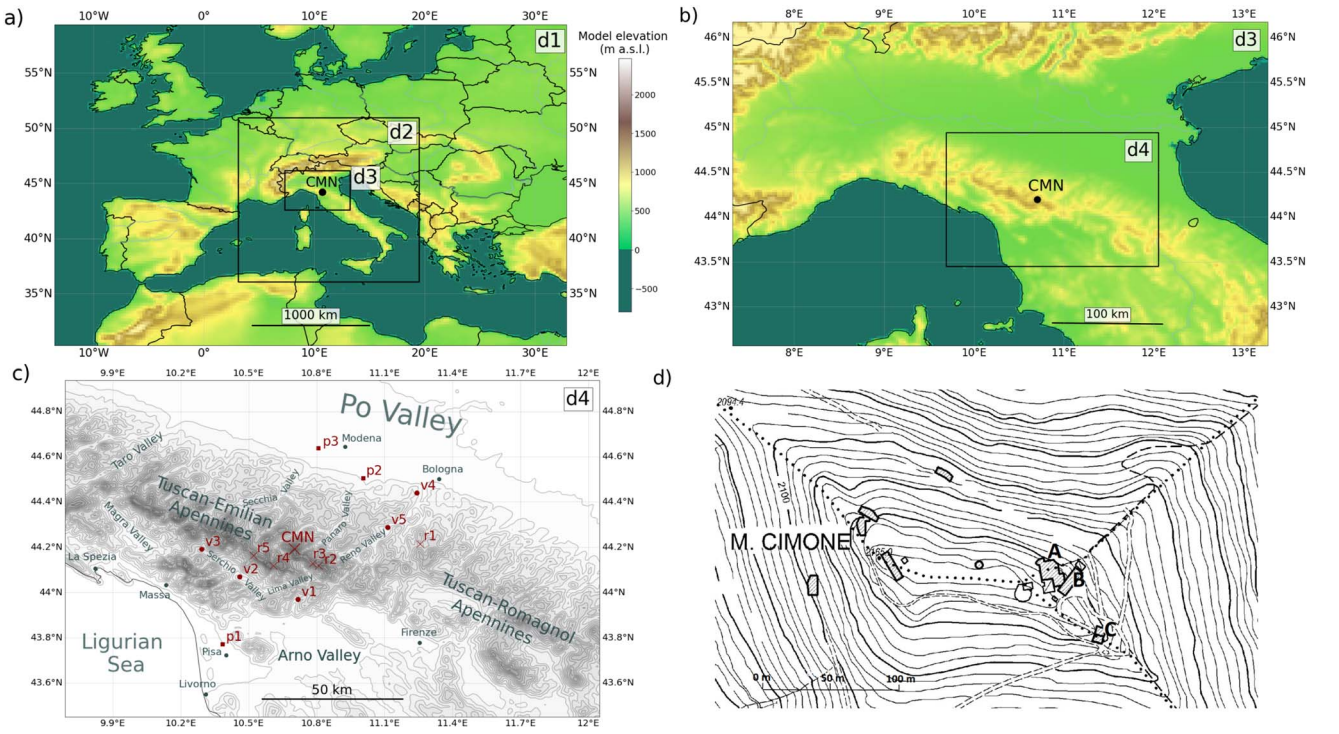

Fig. 1 (a) Position and topography (color shading) of the model domains d1 (27 km resolution), d2 (9 km resolution) and d3 (3 km resolution), (b) zoom-in of domains d3 and d4 (1 km res.) in northern Italy, (c) zoom-in of domain d4 showing the location of the operational stations used for the meteorological evaluation of the model; grey contours represent altitude isolines with a spacing of 100 m. Red symbols and text indicate the considered sites ("p" refers to plain sites, "v" to valley sites and "r" to ridge sites), including Mt. Cimone (CMN). The figure includes relevant toponyms of the area such as valleys and cities. (d) Orography of the summit of Mount Cimone. Isoline interval is 5 m. A, B and C indicate the location of the CAMM meteorological instrumentation, the CNR meteorological instrumentation, and the CNR "Ottavio Vittori" observatory, respectively (source: Emilia–Romagna Geo-portal, see https://geoportale.regione.emilia-romagna.it/).

Northern Apennines, at the transition line between two quite different climate regions: continental Europe (northwards) and the Mediterranean Basin (southwards). The main mountain ridge stretches in the NW–SE direction, almost parallel to the Tyrrhenian coast (located 50 km to the SW), with valleys oriented perpendicularly in the north-eastern side and both perpendicularly and in parallel in the south-western side (Fig. 1b and c). The CMN station is located on the round-shaped top of the mountain, with a 360° free horizon. Due to its high altitude and distance from major pollution sources, it represents a strategic platform to study the chemical–physical characteristics and climatology of the free troposphere of South Europe and of the Northern-Central Mediterranean basin. The research site is typically exposed to air-masses from the planetary boundary layer (PBL) from northern Italy (including the Po Valley) during summer day-time, while it is typically representative of the free troposphere during night-time.[25] The site permanently hosts monitoring facilities operated by research and operational institutions in the infrastructures of the Italian Air Force (Centro Aeronautica Militare di Montagna, CAMM), such as the National Research Council (CNR), which operates the "Ottavio Vittori" observatory, a part of the CMN GAW/WMO station located in a smaller facility, approximately 60 meters to the southeast of the main building and 20 m below the altitude of the summit (see Fig. 1d).

3 Data and methods

In July 2017, the CMN station hosted parts of an international field campaign within the framework of ACTRIS-2. This campaign involved detailed measurements of the aerosol chemical composition. For the present modelling study, a simulation of approximately 1 month (plus 10 days of preceding spin-up period) was run to cover the ACTRIS-2 campaign (4th–28th July 2017). During the selected period, the area of CMN was affected by diurnal mountain winds contributing to the transport of pollutants towards higher elevations.[28]

3.1 Observational datasets

3.1.1 Aerosols chemical data. Aerosol chemical speciation monitor (ACSM) measurements were performed at the Ottavio Vittori Observatory. The ACSM measures the non-refractory (NR) sub-micrometer particulate matter mass (*i.e.* material evaporating at 600 °C, including organics, nitrate, sulfate, ammonium and chloride) with an aerodynamic diameter less than 1 μm (PM_1). The practical time resolution was 30 minutes. A thorough description of the ACSM measurements is available in Ng *et al.*[29]

3.1.2 Meteorological data. Meteorological observations at multiple stations were obtained from different institutions (ESI Table A1†). A comprehensive dataset for the month of July 2017 at CMN, including measurements of air temperature, relative humidity, wind speed and wind direction at 1 min resolution, was provided by the National Research Council (CNR). The CNR meteorological instrumentation was located on the roof of the main structure of the meteorological station close to the mountain top, 100 m to the east and 10 m below the summit (see Fig. 1d).

CAMM provided additional meteorological data, including hourly mean values of wind speed and direction, daily mean atmospheric parameters and weather phenomena like fog and heavy rainfall (METeorological Aerodrome Report – METAR code compliant) observed at CMN. These measurements were performed by the CAMM meteorological station, located on the same building and about 10 metres to the west of the CNR instrumentation (Fig. 1d).

Furthermore we collected hourly-averaged measurements of temperature, wind speed and direction at 13 operational weather stations distributed within a radius of about 50 km around CMN and operated by the Regional Environmental Protection Agencies of Toscana and Emilia–Romagna (ARPAT and ARPAE, respectively). Fig. 1c reports the geographical distribution of the stations; three of them are located in the lowland (*i.e.*, in Metato, Vignola and Marzaglia), either close to the Ligurian Sea or in the Po Valley, five (namely Sorana, Barga, Piazza al Serchio, Sasso Marconi and Vergato) are located inside valleys of the Apennines, either southwest or northeast of CMN, and five (namely Madonna dei Fornelli, Lago Scaffaiolo, Croce Arcana, Foce a Giovo, Monte Romecchio) are on the mountain crests within a range of 20 km from CMN (except Madonna dei Fornelli, which is 45 km to the east and at lower altitude). The distribution of the sites is not optimal, as they leave some areas without a good horizontal and elevation coverage, especially northeast of CMN. However they still allow for a comprehensive evaluation of the meteorological variables in the surroundings of CMN. The thermometer in each station is situated 2 m a.g.l. (above ground level), while the anemometers are located at variable heights (see ESI Table A1†).

3.2 The WRF-CHIMERE model

The WRF-CHIMERE v2020r3 model[27] is a three-dimensional online chemical transport model which accounts for the physical and chemical processes in the Earth's atmosphere, from the emission of pollutants (both from anthropogenic and from biogenic sources) at different elevations, to chained chemical reactions of many chemical compounds, to both dry and wet deposition processes. Along with several other CTMs, CHIMERE serves as a member of the Copernicus Atmosphere Monitoring Service's (CAMS) for operating air quality forecasts in Europe (**https://atmosphere.copernicus.eu/**), it participates in several intercomparison exercises,[30–38] and has been intensively used as a research and prognosis state-of-the-art CTM over the European domain during the last couple of decades. The models (chemical and coupled meteorological models) codes are provided in an open access fashion with a centralized repository freely available at **https://www.lmd.polytechnique.fr/chimere/**(available upon subscription) and are shipped with a complementary set of pre/post processors, in a highly modular environment at the interface with CHIMERE, which facilitates the preparations of anthropogenic emissions especially over the European domain and the handling of large amount of output files.

The chemical scheme used for reproducing the gas-phase chemistry was MELCHIOR2,[39] which includes up to about 120 reactions with updated reaction rates and reduces the computing time compared to more detailed schemes available in the model such as SAPRC.[40] For the inorganic aerosol constituents, the ISORROPIA thermodynamic model was used to calculate the partitioning between gas and particle phase.[41] The total aerosol mass was distributed into 15 bins ranging from 10 nm to 40 μm in particle diameters using a logarithmic sectional distribution approach, accounting for coagulation process[42] as well as binary nucleation of sulfuric acid (H_2SO_4) and water.[43] The organic aerosol (OA) fraction in the model is treated using the volatility basis set (VBS) scheme.[27,44] Oxidation products of anthropogenic and biogenic volatile organic compounds (AVOCs and BVOCs, respectively) are distributed into four classes of volatility at a saturation concentration of 1, 10, 100, and 1000 μg m^{-3} respectively (at 300 K), with different mass yields for low-NO_x and high-NO_x conditions based on Cholakian *et al.*[45] and their aging processes set to a reaction rate of 1×10^{-11} molecule^{-1} cm^3 s^{-1} for ASOA[44,46] and 4×10^{-12} molecule^{-1} cm^3 s^{-1} for BSOA.[47,48] First and second oxidation of semi-volatile volatile organic compounds (SVOCs) from primary emissions (POA) are allowed to react with a reaction rate of 4×10^{-11} molecule^{-1} cm^3 s^{-1}, leading to additional formation of secondary organic aerosol (SOA).

Meteorological fields were obtained from the WRF regional model (v3.71)[49] forced with data from the National Centers for Environmental Prediction (NCEP) Climate Forecast System (CFSv2; **http://www.ncep.noaa.gov**, last access: 01 May 2023) with a temporal resolution of 6 h, an horizontal resolution of 1°, and with the coarse domain nudged towards the reanalysis data (every 6 hours, *i.e.* surface grid nudging). Simulations were performed using the Rapid Radiative Transfer Model (RRTM) radiation scheme,[50] the Thompson aerosol-aware microphysics (MP) scheme to treat the microphysics[51] the Monin–Obukhov surface-layer scheme (Janjic, 2003), and the NOAA Land Surface Model scheme for land surface physics.[52] The boundary-layer option was the Mellor–Yamada–Janjic (Eta) turbulent kinetic energy (TKE) scheme. The overall WRF model configuration used here largely builds upon previous applications of the WRF model over other mountain regions of the Himalayan chain.[10,53] For the latter application, after extensive testing, an adaptive time step was enabled to avoid unrealistic vertical velocities in proximity of mountain peaks and to satisfy the Courant–Friedrichs–Lewy (CFL) condition, which was however not necessary for the simulation over the Apennines presented here. Additionally, in this case the WRF simulations were performed on 33 vertical sigma layers rather than 60 as in our previous Himalayan applications, in order to constrain the model output and computation resources during the 1 month run.

The most important model configuration options used in this study are summarized in ESI Table B1.†

The model was run from the 24th June 2017 to the 28th July 2017 and included a spin-up period of 10 days.

3.2.1 Model emissions input data. Anthropogenic emission fluxes of nitrogen oxides (NO_x), sulfur dioxide (SO_2), black carbon (BC), organic carbon (OC), carbon monoxide (CO), ammonia (NH_3) and non-methane volatile organic compounds (NMVOCs) were retrieved from the CAMS datasets for the year 2017 at 0.1 × 0.1° (~10 km) horizontal resolution and hourly resolved over the investigated period (July 2017), and additionally down-scaled to a higher resolution grid (1 km) using proxy data as top-down approach (a simple mass-conservative algorithm funnelling industrial and traffic emissions into grid cells containing industrial sources or the roadmap). Biogenic emissions of NO, isoprene, limonene, α-pinene, β-pinene, ocimene, and humulene (representing the lumped class of sesquiterpenes) were prepared using the MEGAN model version 2.1.[54] Emission rates of 15 plant functional types (PFTs), at an original horizontal resolution of 0.008° × 0.008° (~1 km), were re-gridded to match the resolution of the domains in use for the meteorological fields. Standard emission rates are adjusted by MEGAN according to several environmental factors, based on local radiation and temperature values, as well as other variables, such as the leaf area index (LAI).[54] The MEGAN input dataset embedded in CHIMERE is based on the year 2013 but is currently being updated for follow-up applications in regions largely affected by biogenic emissions. Initial and boundary conditions of aerosols and gas-phase constituents were retrieved from the climatological simulations of LMDz-INCA3 [55] and the Goddard Chemistry Aerosol Radiation and Transport (GOCART) model.[56] For aerosol species, in particular, the model includes inorganic species such as fine (diameter < 2.5 μm) and coarse (diameter > 2.5 μm) nitrate, ammonium, sulfate, dust, as well as organic carbon (OC) and black carbon (BC).

3.2.2 Evaluation metrics. The meteorological fields obtained from WRF simulations were evaluated comparing the near-surface simulated temperature, wind speed and direction with observed values measured at CMN as well as at the other operational stations (Section 3.1.2). In particular, modeled values were extracted from the grid point closest to each station, identified through a simple algorithm comparing the coordinates of the station and the domain mesh. The surface wind in the model was taken at 10 m above ground, while wind observations were taken at different heights, depending on the sites. The modeled wind speed was therefore extrapolated to the correct anemometer height assuming a logarithmic wind profile with neutral stratification (Stull, 1988), as in eqn (1):

$$u(z_A) = u(z = 10) \cdot \frac{\ln(z_A/z_0)}{\ln(10/z_0)} \quad (1)$$

where $u(z_A)$ and $u(z = 10)$ are the wind speeds at anemometer height and at 10 m a.g.l., respectively, and z_0 is the roughness length, extracted for each model cell from the 1 km resolution domain. No adjustment was applied to the modeled wind direction. Both the modeled and observed temperatures were at 2 m above the surface level, but the modeled value was corrected for the elevation mismatch between the model domain and the actual surface, assuming a mean tropospheric temperature lapse rate of $\gamma = -6.5$ K km^{-1}, as in eqn (2):

$$T_c = T + \gamma \cdot \Delta Z \quad (2)$$

where T_c (in °Celsius) is the corrected modeled 2 m temperature, ΔZ is the elevation difference, and T is the modeled temperature on the model topography.

The model evaluation was based on the Root Mean Square Error (RMSE), the Mean Bias Error (MBE) and the correlation coefficient (R), computed as in eqn (3)–(5) respectively:

$$\mathrm{RMSE} = \sqrt{\sum_{i=1}^{N} (\mathrm{obs}_i - \mathrm{mod}_i)^2} \quad (3)$$

$$\mathrm{MBE} = \sum_{i=1}^{N} (\mathrm{obs}_i - \mathrm{mod}_i) \quad (4)$$

$$R = \frac{N\sum_{i=1}^{N}(\mathrm{obs}_i \mathrm{mod}_i) - \left(\sum_{i=1}^{N}\mathrm{obs}_i\right)\left(\sum_{i=1}^{N}\mathrm{mod}\right)}{\sqrt{\left[N\sum_{i=1}^{N}(\mathrm{obs}_i{}^2) - \left(\sum_{i=1}^{N}\mathrm{obs}_i\right)^2\right]\left[N\sum_{i=1}^{N}(\mathrm{mod}^2) - \left(\sum_{i=1}^{N}\mathrm{mod}\right)^2\right]}} \quad (5)$$

Here, obs_i and mod_i refer respectively to the observed and to the modeled value extracted in the closest model cell at the same time step, while N represents the number of model-observation data couples at a time resolution of 1 hour, *i.e.*, the total number of hourly time steps in the investigated period. To compare it with observed PM_1 mass, modeled aerosol mass was summed over the model bins with median diameter < 1 μm.

4 Model evaluation

4.1 Synoptic context

Climatologically, the month of July 2017 was warmer and dryer than the 1981–2010 average over southern Europe. The precipitation pattern was more scattered, with some areas in the Mediterranean (south of the Iberian Peninsula and central Mediterranean) receiving more rain than usual (**https://climate.copernicus.eu/climate-bulletins**). In Italy, the northern Apennines region, *i.e.* Tuscany and Emilia–Romagna, was affected by frequent and short heatwaves, interrupted by cooler periods. The average temperature was 1.5 °C warmer and precipitation was 34 mm lower (−65%) than the 1961–1990 climatology.[57] The modeled synoptic conditions and large-scale flow during the investigated period were analysed and divided in 6 sub-periods (ESI Fig. A1†):

1. 4th–9th July: a wide African anticyclone, enhanced by the presence of a cut-off cyclone and co-located upper level low over Portugal, progressively extended northward covering most of the Mediterranean basin, causing calm wind and fair weather over Italy until the 9th (ESI Fig. A1a†).

2. 10th–12th July: The afore-mentioned low-pressure system weakened and moved towards the Alps. At upper levels a new larger trough moved in from west, causing strong westerly winds over the western Mediterranean and the Italian Tyrrhenian cost (ESI Fig. A1b†), reaching a peak on the 11th.

3. 13th–17th July: a new upper-level trough passing over the UK moved towards the south-east, bringing cooler air in the lower atmosphere, affecting initially eastern Europe and later the entire Balkan region, before losing intensity over Greece. Concurrently, a high developed over north-western Africa causing a strong pressure gradient oriented north-south over France and northern Italy (ESI Fig. A1c†).

4. 18th–20th July: a second anticyclonic phase influenced the western/central Mediterranean, with weak westerlies prevailing over Corsica and central-northern Italy (ESI Fig. A1d†).

5. 21st–26th July: anticyclonic conditions were interrupted by a low-pressure system reaching Great Britain and extending further south in the following days with persisting intensity. At the same time a strong high formed over Tunisia (23rd), resulting in strong westerly winds at CMN (ESI Fig. A1e†).

6. 27th–28th July: western Europe was affected by westerly winds at higher and lower levels caused by an Atlantic low facing the British islands and a high-pressure system developing over Morocco (ESI Fig. A1f†).

4.2 Analysis of near-surface meteorological dynamics in the high-resolution domain

This section presents the meteorological evaluation of the model simulations at local scale (1 km) over the northern Apennines region corresponding to domain d4 (Fig. 1). The discussion proceeds from low to high altitude, first considering a subset of sites located to the south-west of the Apennines ridge (Section 4.2.1), then sites located to the north-east (Section 4.2.2), and finally stations located on the mountain ridges, including CMN (Section 4.2.3). Table 1 shows the statistical

Table 1 Root Mean Square Error (RMSE), mean bias error (MBE) and correlation coefficient (R) calculated as in Section 3.2.2 for air temperature (T (°C)) and wind speed (ws (ms^{-1})) in all considered sites (and subsets of sites) during the study period

		T (°C)			Ws ($m\ s^{-1}$)		
ID	Site name	RMSE	MBE	R	RMSE	MBE	R
p1	Metato	2.55	1.34	0.90	1.17	0.67	0.78
v1	Sorana	1.66	0.06	0.89	0.71	−0.07	0.55
v2	Barga	4.07	2.59	0.88	0.94	0.16	0.47
v3	Piazza al Serchio	2.24	0.62	0.90	0.78	−0.11	0.65
Average stations on the southwestern slope		**2.63**	**1.15**	**0.89**	**0.90**	**0.16**	**0.62**
p2	Vignola	5.29	4.19	0.84	1.68	0.43	0.19
p3	Marzaglia	4.36	2.90	0.83	1.57	−0.06	0.27
v4	Sasso Marconi	2.35	1.39	0.90	1.89	0.09	0.31
v5	Vergato	4.46	3.28	0.89	1.38	0.58	0.61
Average stations on the northeastern slope		**4.12**	**2.94**	**0.87**	**1.63**	**0.26**	**0.35**
r1	Madonna dei Fornelli	2.24	1.32	0.85	1.96	−0.79	0.61
r2	Lago Scaffaiolo	1.91	−0.02	0.77	3.28	−0.03	0.48
r3	Croce Arcana	—	—	—	2.88	1.56	0.50
r4	Foce a Giovo	1.79	0.10	0.80	3.71	0.74	0.17
r5	Mt. Romecchio	—	—	—	2.99	0.97	0.52
CMN	Mt. Cimone	1.48	−0.22	0.88	4.83	1.45	0.16
Average ridge stations		**1.89**	**0.30**	**0.83**	**3.28**	**0.65**	**0.41**
Average all stations		**2.86**	**1.46**	**0.96**	**2.13**	**0.40**	**0.45**

results for each site and for each subsets of stations. Given the number of sites, we report here only figures of the most representative ones for each subset, to highlight differences between investigated areas, including time series and mean diurnal cycles of the investigated variables. However, when considered relevant, notable features of specific sites (*e.g.*, primarily the site of CMN) are included in the analysis. The complete set of figures is included in ESI.†

4.2.1 Sites located on the south-western side. We present here the plain station of Metato (p1 in Fig. 1), at 3 m above sea level, approximately 10 km from the Ligurian Sea coast, and the valley stations of Sorana, Barga and Piazza al Serchio (v1, v2 and v3, respectively), all at altitudes ranging from 270 m to 660 m a.s.l. Data from the stations of Metato (p1) and Sorana (v1) are shown in Fig. 2, while Barga (v1) and Piazza al Serchio (v3) are shown in Fig. A7 and A8 in ESI.†

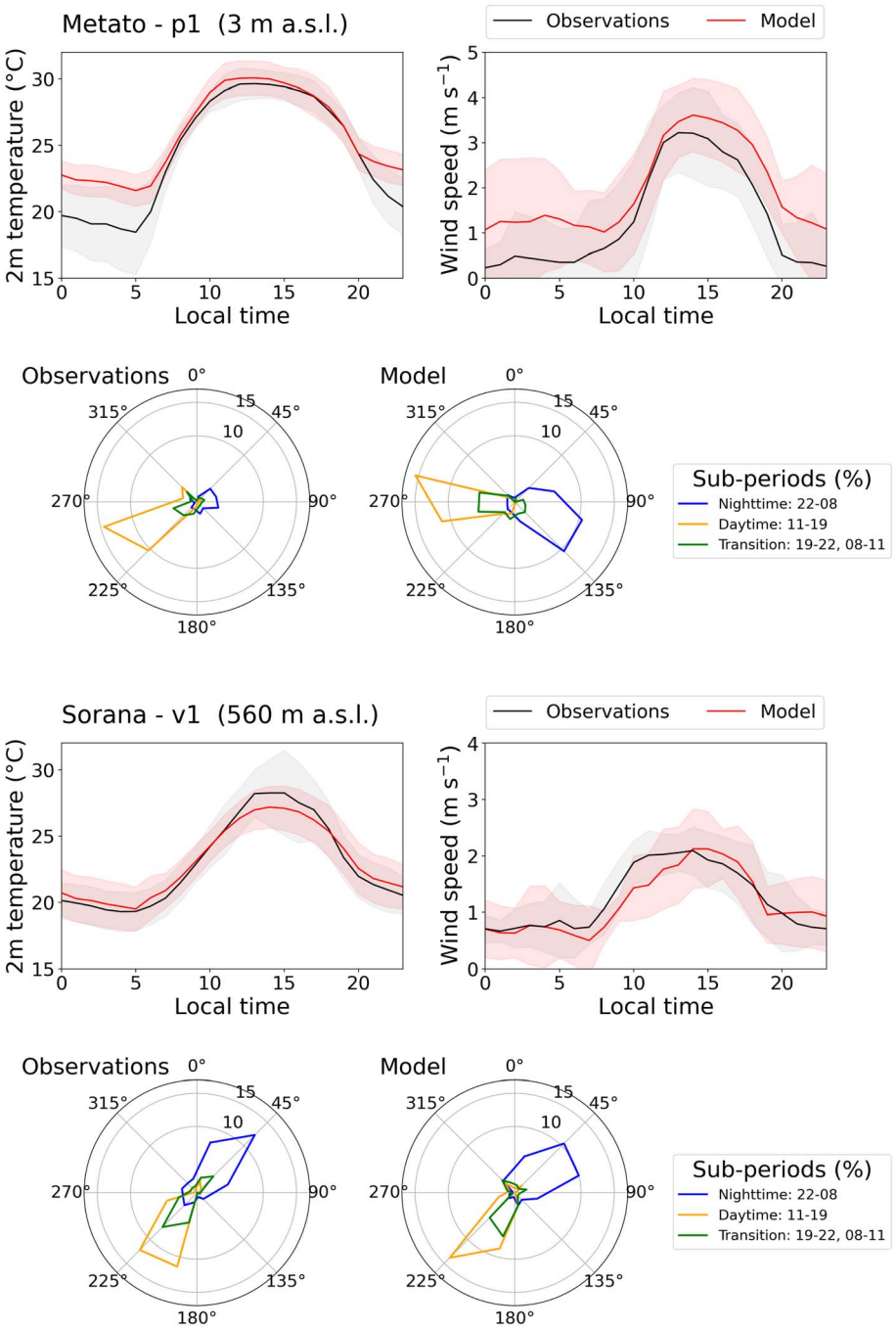

Fig. 2 Modeled (red lines) and observed (black lines) values for the stations of Metato (p1, top panel) and Sorana (v1, bottom panel) reporting the average diurnal cycle (in local time, LT) for air temperature (top-left, °C) and surface wind speed (top-right, m s^{-1}). The shaded area indicates the $\pm\sigma$ (standard deviation) range. Bottom plots report the time frequency (% of all period) on a polar plot of wind directions sub-divided in daytime, nighttime and transition period for the observed (bottom-left) and modeled (bottom-right) wind at anemometer height.

At Metato (p1) observations show a strong diurnal cycle in temperature, wind speed and direction, indicating the presence of a sea-breeze circulation developing between the Ligurian Sea and the adjacent plain. Consistently, the wind generally blows from the west during daytime, reaching a maximum intensity at 13:00 (around 3 m s^{-1}, with only few days exceeding 4 m s^{-1}), while nights are characterized by either weak land-to-sea winds or calm conditions. In general, the model output is in line with measurements, both in terms of temperature, wind speed and direction (Fig. 2). The intensity of the sea breeze is slightly overestimated by the model (MBE = 0.67 m s^{-1}), but the timing of the onset (10:00 LT) and of the return to calm wind conditions (20:00 LT) are correctly reproduced. The model also overestimates the wind intensity at night, and exhibits a slight shift towards north (by about 30°) of the prevailing wind direction. Temperature is reproduced by the model, but an overestimation of about 3 °C occurs during nocturnal hours, resulting in an overall MBE of 1.34 °C.

At Sorana (v1), Barga (v2) and Piazza al Serchio (v3), very similar patterns are observed, with less pronounced diurnal

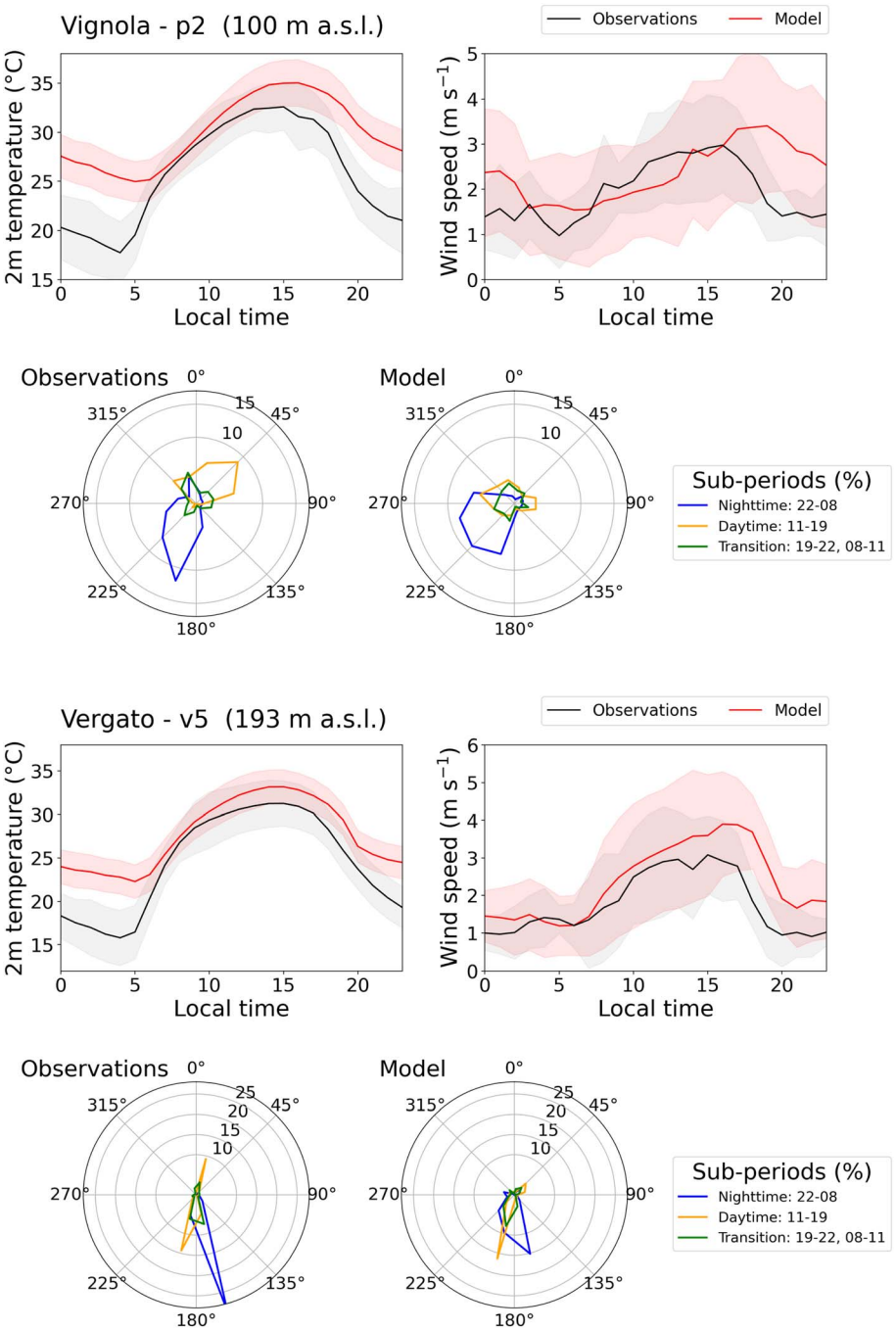

Fig. 3 Modeled (red lines) and observational (black lines) data as in Fig. 2 but for the stations of Vignola (p2) and Vergato (v5).

variations in temperature and wind. During day-time, these sites are influenced by thermal breezes with up-valley flows between 2 m s^{-1} and 3 m s^{-1}, likely sustained by the sea-breeze in the underlying plain (Fig. 2). The wind direction pattern is associated with the local topography (*i.e.*, following the direction of the valley floor): during the day, in Sorana (v1) the flow is mainly from south-west, and in Barga (v2, see ESI Fig. A7†) from south-east, while for Piazza al Serchio (v3, see ESI Fig. A8†) it blows from the adjacent valley located west of the station. Conversely, at night, the wind turns downvalley. The simulated wind speed in the three valley sites closely follows the observed diurnal cycle, with timing and wind intensities in remarkably good agreement with the measurements and with reasonably low RMSEs and MBEs. Also, as shown in Fig. 2, wind direction and temperature are very well reproduced (notably, station v2 displays a comparably high positive MBE in temperature). This situation persists throughout the whole simulation period, even on days with strong synoptic winds aloft, *i.e.*, the diurnal pattern, both in the model output and in the observations is not disrupted by the large-scale flow measured at higher altitudes on specific days during the study period.

4.2.2 Sites located on the north-eastern side. We report here a comparison for plain and valley sites (p2, p3, v4, v5) located northeast of CMN at altitudes ranging from 54 m to 275 m a.s.l. Among these, Vignola (p2) is near the inlet of the Panaro valley, while Marzaglia (p3) is in the Po plain, about 10 km from the Apennines feet (see Fig. 1). Unfortunately, no data was retrieved from sites on the valley floor of the Panaro valley (which directly connects CMN to the Po Plain, see Fig. 1). However ESI data† were obtained from the stations of Sasso Marconi (v4) and Vergato (v5) located in the adjacent Reno valley, a few kilometers south-east, respectively 7 km and 25 km from the valley inlet (Fig. 1). Fig. 3, shows data from the stations of Vignola (p2) and Vergato (v5), while Fig. A6 and A9, in ESI,† refer to the stations of Marzaglia (p3) and Sasso Marconi (v4). For these four stations, the observed amplitude of the diurnal temperature cycle is larger compared to the stations on the southwestern side (maxima reaching 32 °C), because of a weaker mitigating effect of the sea (Fig. 3). The model substantially overestimates the temperature (MBEs > 2.90 °C) at night, especially in the plain stations, where the difference with measurements often exceeds 5 °C. In the Reno valley, the simulated temperature is in better agreement with measurements, but there is still a significant mismatch, especially at Vergato (see Table 1).

The observed wind pattern for stations located at an outer position compared to the mountain range (p2, p3, see Fig. 3 and A6 ESI†) is coherent with a daily-periodic mountain wind system, with a maximum plain-to-mountain wind around 16:00 and the opposite situation, associated with weaker intensity, during nighttime (Fig. 3). Unlike stations on the south-western side of the Apennines, the observed wind direction is scattered on the wind rose, without definite directions associated to either daytime or nighttime flows, as typical of open topography compared to valley locations. The comparison of the diurnal patterns of wind speed indicates scenarios comparable to those obtained for stations located on the southwestern side, but with a lower correlation (0.35 *vs.* 0.62) and modest overestimation of the wind intensity starting from 15:00 to 2:00 (MBE < 0.30 m s^{-1}). Although the model can reproduce the general day-to-day evolution of the prevalent wind direction (see ESI Fig. A4 and A6†), in the same plain stations (p2 and p3) there are significant discrepancies in the diurnal pattern of the wind direction (Fig. 3), with the observed daytime northerly (upslope) component underestimated in the model, with few exceptions for specific days.

An interesting feature is found in Sasso Marconi (v4), near the inlet of the Reno valley (see Fig. 1), where observations and model output are in evident contrast, with the former showing evidence of a diurnal up-valley (northeasterly) wind developing on most days, while the latter displaying winds aligned with the valley floor, but downvalley (southerly), towards the Po valley (ESI Fig. A9†). Surprisingly, 15 km further south, at Vergato (v5), both model and observations agree on a predominant "reversed" flow oriented towards the Po valley (thus downvalley), developing in the afternoon for a significant fraction of the analysed days (Fig. 3). This is counter-intuitive from a theoretical standpoint, given the orientation and gradient of the valley floor, but might be explained by the diurnal surface wind pattern in the model, which implies intense westerly wind blowing from the Ligurian Sea, affecting the southwestern side of the Apennines and extending over the ridgeline where the mountain range elevation is lower (as discussed in details later in Fig. 7). The southerly wind component in the Reno Valley in the model might therefore result from this circulation (note that the mountain gaps connecting the Po valley and the Arno valley in this area are lower compared, for instance, to the area of CMN).

4.2.3 Sites located on the Apennines ridge line. In addition to observational data obtained directly from CMN, four stations (namely r2, r3, r4, r5) were considered over the Apennines ridge within a radius of 15 km from the Mt. Cimone top at altitudes ranging from 1591 to 1794 m a.s.l. Additionally, data were retrieved from station r1, located at 900 m a.s.l. on a secondary crest about 50 km east of CMN. Fig. 4 and 5 allow comparing data from the stations at Lago Scaffaiolo (r2) and Mt. Cimone (CMN), respectively, while Fig. A10–A13, in ESI,† show data from the other ridge stations. In contrast with the plain and valley ones, ridge stations are exposed to large-scale winds and are frequently in free tropospheric conditions. As a consequence, the evolution of the local near-surface variables is largely influenced by the synoptic situation, resulting in similar patterns at all the ridge stations, changing on timescales ranging from one day to one week. All stations recorded high wind speed during 3 distinct periods: from the 10th to the 12th, from the 15th to the 17th and from the 20th to the 28th of July, corresponding respectively to phases (2), (3) and (5) of the synoptic evolution described in ESI Fig. A1.† On the other hand, lower wind speeds affected the ridge during phase (1) (from the 4th to the 9th) and (4) (from the 18th to the 20th of July), when anticyclonic conditions persisted over southern Europe. Consistently, wind direction oscillated between northwest and southwest, except for the 16th and 17th, when the flow was northerly.

Here we first discuss the results for all the ridge stations with the exception of CMN, which presents some distinctive features

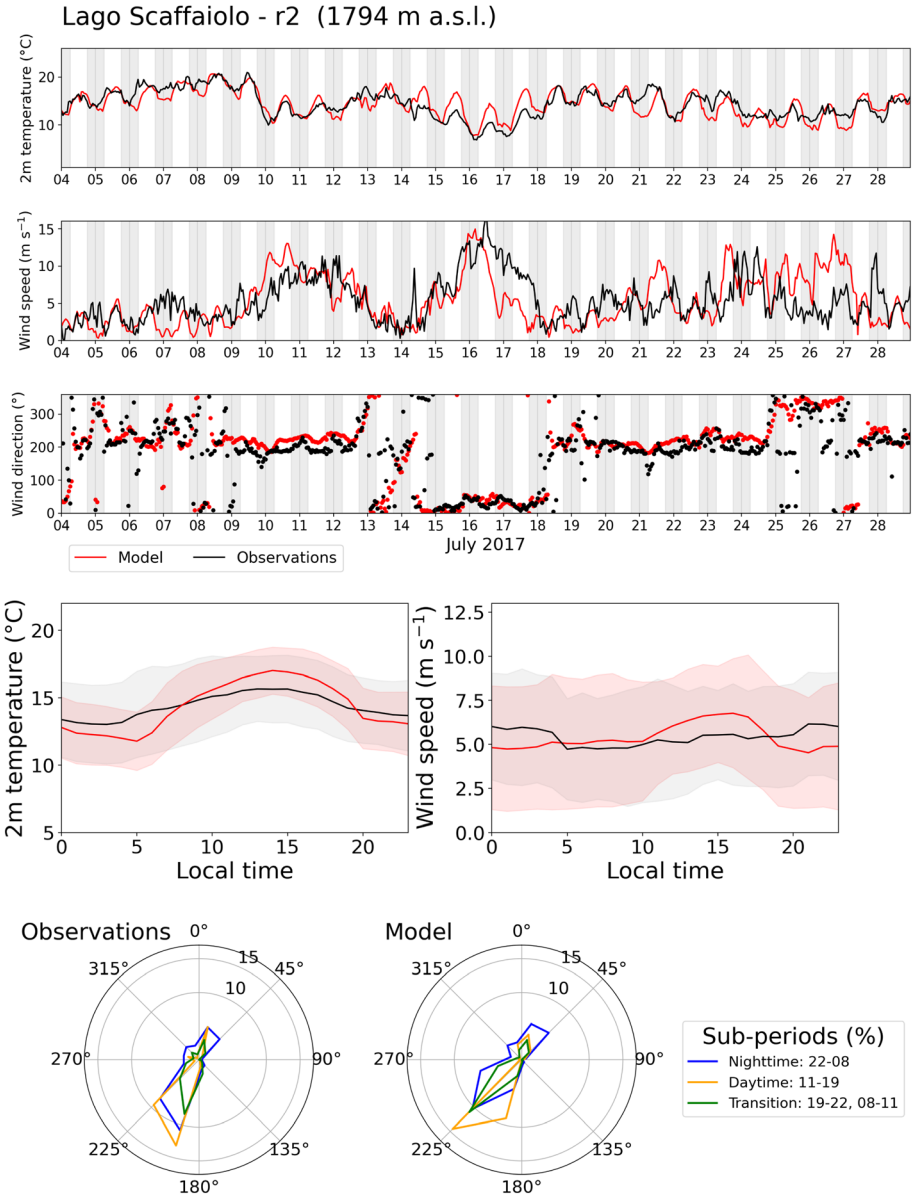

Fig. 4 Modeled (red lines) and observational (black lines) data for the station of Lago Scaffaiolo (r2). Top panels report the timeseries of air temperature (°C), wind speed (ms^{-1}) and direction (°). Bottom panels report the corresponding average diurnal cycle and wind direction frequencies for the same period, as in Fig. 2.

and is analysed in detail afterwards. Results indicate a good model skill in reproducing the wind direction on the Apennines ridgeline, with small systematic angle errors depending on the specific site (*e.g.*, at r5: negative bias of 50°, see ESI Fig. A13†). A satisfactory agreement between model and observations was also found for the wind speed (slight overprediction by the model, average MBE = 0.65 m s^{-1}), which reproduces the general observed day-to-day trend, with substantial differences only on the 16th–17th (negative or positive bias depending on the site) and on the 25th–26th (positive bias, see Fig. 4 and A10–A13 ESI†).

Diurnal variations appear less regular than the one observed for stations located at lower altitude. The simulated temperature, specifically, (available only at r1, r2 and r5), exhibit a more pronounced diurnal variation compared to observations, overshooting on average the maximum and minimum measured values, though without a constant bias during the simulation (see *e.g.* Fig. 4) and with a relatively small MBE (0.30 °C). Besides, discrepancies between the simulation and observational data appear in the average diurnal evolution of the wind speed, with slightly higher values during nighttime in measurements (especially for r2, Fig. 4), and, conversely, a remarkable afternoon maximum in the model (r4 represents an exception to this pattern), which results in an average RMSE (3.28 m s^{-1}) much larger than the one for plain and valley stations. The diurnal evolution indicated by observations is

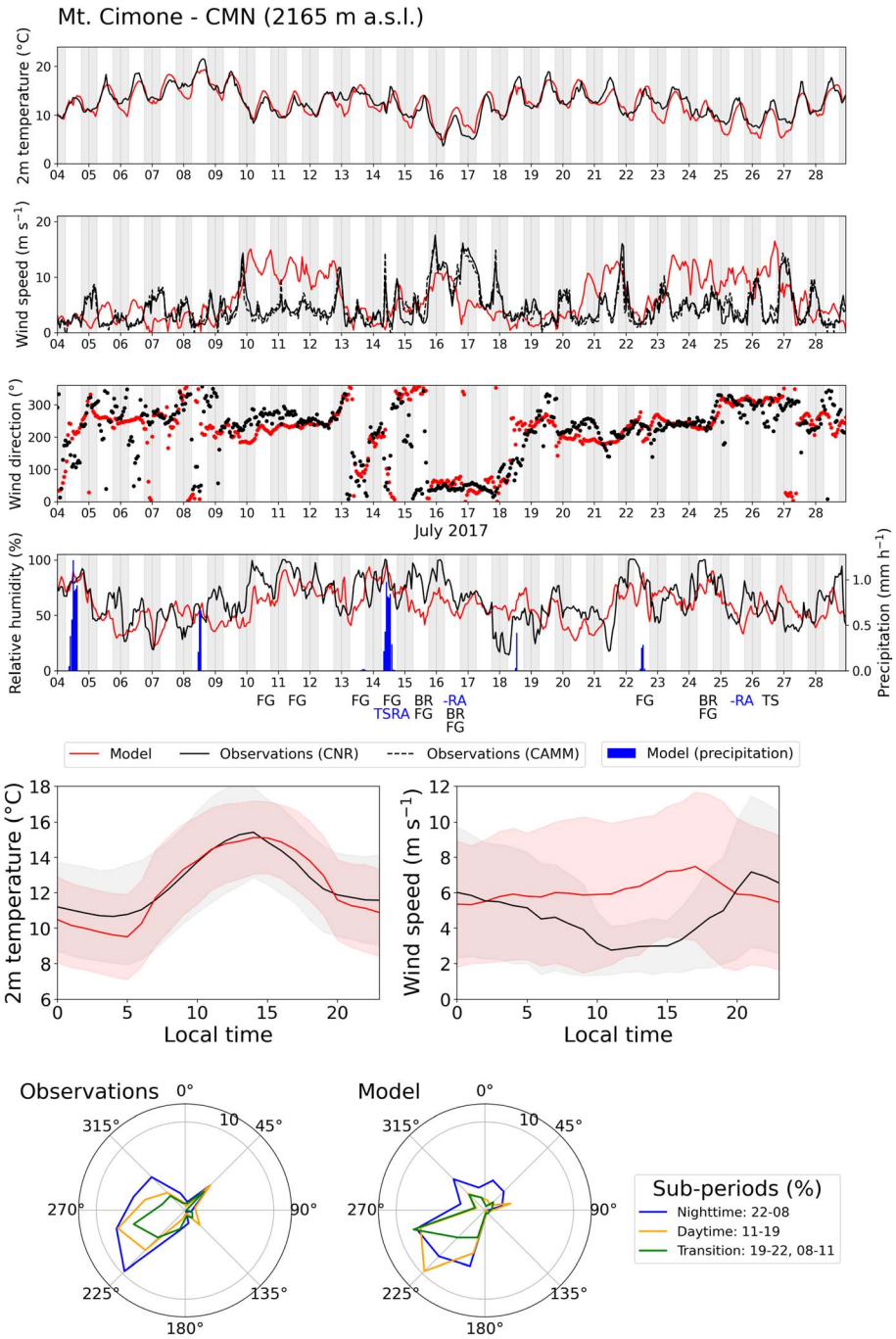

Fig. 5 Modeled (red lines) and observational (black lines) data as in Fig. 4 but for the Mt. Cimone (CMN) station including also relative humidity (%) and precipitation (kg h^{-1} m^{-2}).

consistent with a nocturnal shallow boundary layer over mountain tops and ridgelines, which can be affected by high-speed tropospheric winds at night and conversely be protected by the mountain PBL during the day. On the other hand, the peak occurring in the late afternoon in the model is likely due to slope winds developing at lower altitudes and eventually reaching the ridgeline, venting PBL air into the free-troposphere. Note that, consistently with this hypothesis, there is a temporal shift of few hours in the modeled wind speed when comparing plain stations (peak at 13:00–14:00), valley stations (peak at 14:00–15:00) and ridge stations (peak at 16:00). As discussed below, this different behavior between model and observations might be attributed to the approximated representation of the orography in the model. Moreover, an accurate visual inspection of the entire period (see Fig. 4 and A10–A13 ESI†) also reveals two distinct situations for unperturbed and perturbed conditions respectively:

Under calm conditions (most notably during 4th–9th, and 18th–19th), observations and model output generally agree, showing a visible afternoon peak and low wind speed at night.

This is most evident on the 5th and on the 19th for most of the ridge stations. On the other hand, under disturbed conditions, irrespectively of the wind direction, observations show a variable combination of nocturnal peaks and daytime peaks, with one of the two situations predominant at some sites. In particular, the afternoon peak is usually seen in the simulated wind speed (*e.g.*, 10th–12th in Fig. 4), sometimes overestimating observations, while the comparison of the nocturnal peaks is highly dependent upon the station under consideration.

We consider now specifically the case of CMN, which presents a slightly different topography from the ones of stations previously discussed as the mountain summit is a few hundreds of meters higher than the ridgeline and constitutes an isolated round-shaped peak. In this case, the analysis benefited from additional data provided by the weather service of the Italian Air Force (specifically, the Centro Aeronautica Militare di Montagna, CAMM, located on Mt. Cimone) and includes also relative humidity (RH) and precipitation. Concerning temperature ranges, during the investigated period, air temperature at CMN varied between 3.7 °C and 21.6 °C, with a diurnal temperature range of approximately 5 °C (irregular diurnal variations on few specific days, *e.g.*, the 13th, are likely related to partially overcast skies). The model is able to reproduce the daily temperature evolution, but shows a general underestimation of the daytime maximum and nighttime minimum (Fig. 5), especially in the first few days and in the second half of the simulation period, resulting in the station with the most negative temperature MBE (−0.22 °C). High RH values are measured on the 10th–16th and 22nd–24th periods, consistently with the unstable conditions driven by the large-scale circulation. The observed diurnal pattern of RH varies throughout the investigated period: in general, a nocturnal maximum in correspondence of the temperature minimum is well visible under disturbed conditions (*e.g.*, in the periods 10th–12th, 14th–16th or on the 22nd), while an afternoon maximum associated with the lowland PBL transport can be identified in clear-sky days (note for example the 5th–8th period or the 19th). The two patterns are sometimes combined in a double-peak daily profile (11th or 22nd). The simulated RH underestimates the measurements for most days, especially in low-pressure conditions (notably, on the 10th, 11th and on the 22nd). Nevertheless, the daily trend and the diurnal evolution are reproduced in the model with acceptable accuracy (mean relative error = −14.5%). Precipitation and other weather phenomena are recorded at CMN on a daily basis and are reported for the study period in Fig. 5 according to the METAR convention (*e.g.*, frequent fog events are identified in 30% of the days, mainly between the 10th and the 16th). The simulated precipitation, reported as mm h^{-1} in Fig. 5, shows scarce agreement with observed events, except for a thunderstorm event occurring on the 14th.

The comparison of the wind direction at CMN reproduces the same scenario observed at the ridge stations: the relatively constant wind direction resulting from the large-scale circulation is correctly reproduced by the model. The comparison of the wind speed, however, exhibits remarkable discrepancies, unlike other ridge sites, resulting in the highest RMSE and the lowest correlation among all the considered stations (see Table 1). In particular, a comparison of Fig. 4 with Fig. 5 shows that the strong winds (>10 m s^{-1}) measured by the surrounding ridge stations during the periods 10th–12th and 23rd–24th are not detected by the anemometer installed at CMN (which measured ∼5 m s^{-1}), except for a brief initial wind gust, which rapidly disappears, (see the night between the 9th and the 10th). All the other ridge stations described above recorded high wind speeds, regardless of the elevation and relative position with respect to CMN. Moreover, at CMN, the model does predict large wind speeds in those periods, with intensities comparable to the ones in the other ridge stations. In addition, the periods when this mismatch occurs are characterized by wind blowing steadily from the WSW direction, while for other angles the average error is much smaller (ESI Fig. A14†). This contrasting behaviour suggests that the location of the anemometer on the roof of the building might be affected by disturbances, such as wake effects from other structures or obstacles located upwind. Indeed (as shown by Fig. 1d), several antennas taller than the roof are installed west of the main building where the CNR anemometer is located. Wind speed data from the CNR instrumentation were compared to data from the nearby CAMM anemometer, located less than 10 m west of the CNR one, on the roof of an adjacent building and nevertheless aligned in the direction of the assumed obstacles (see ESI Fig. A15†). The timeseries of data collected by the two instruments compare almost identically: Fig. 5 shows no major difference in the wind at the two places, and suggests that the two anemometers are representative at least of an area with a diameter of about 10 meters, although neither of them is in an optimal position to represent the entire mountain summit.

A second major discrepancy between observed and modeled wind speed is found in the average diurnal pattern (Fig. 5). In line with the conditions described for the other ridge stations, the observed wind speed peaks at night, while the modeled maximum occurs in the late afternoon (note that this pattern persists even after removing from the dataset the days of large wind speed overestimation discussed above). A plausible reason, explaining both major discrepancies at CMN (*i.e.*, both the overestimation of the wind from WSW and the anti-correlated diurnal variation) consists in the representation of the topography in the model domain, which might impact the simulated strength and structure of wind phenomena induced in proximity of the mountain top. As already discussed, and reported in ESI Table A1,† even at a 1 km grid-spacing, the model topography exhibits rather large local deviations from the Earth's surface (obtained from a digital terrain model at 10 m resolution). Moreover, as depicted in ESI Fig. A16,† the complex terrain area within a few tens of km from CMN is particularly modified by the smoothing required to ensure numerical stability, with filled valley floors and cropped ridges (a maximum mismatch of −291 meters occurs at the summit of Mt. Cimone). This most likely reflects in a misrepresented terrain forcing on the flow. For instance, the elevation and shape mismatch between model and real topography could affect the level of exposure of single sites to free-tropospheric winds (*e.g.*, in a smoothed model scenario, peaks and ridges are less protruded compared to other peaks) or influence the

PBL structures, accelerating or slowing down the flow impinging on the mountainsides. More specifically, for CMN, the mountain summit could shelter the measuring site from wind from WSW, an effect that could not be captured in the current model configuration, as the distance between the station and the mountain top is only 120 meters. Also, local features of the summit might affect the wind speed detected on the roof of the station. Note that, instead of man-made structures, we refer here to small scale landforms constituting the three-dimensional shape of the top of CMN, which cannot be represented at the current resolution.

4.3 Aerosol concentrations and chemical composition at CMN

In this section we discuss the concentration and chemical composition of the non-refractory PM_1, including nitrate (NO_3-), ammonium (NH_4^+), sulfate (SO_4^{2-}) and organic aerosol (OA). A comparison of hourly values of observed and modeled concentration at CMN is shown in Fig. 6. In ESI Fig. B1† we further report the modeled mean spatial distribution of the main chemical components over domain d3 (3 km resolution) to facilitate the presentation of the results.

The analysis revealed a satisfactory agreement between the observed and the modeled average PM_1 mass fractions, although differences in the model performance depend on the specific component under consideration. Specifically, the modeled sulfate (SO_4^{2-}) concentration was found to be in good agreement with the ACSM data, with a mean concentration of 1.12 ± 0.73 μg m^{-3} and 0.89 ± 0.39 μg m^{-3} in the model and in observations, respectively, implying a relative error of 21%, and with a correlation coefficient of 0.59. The modeled weekly trend and diurnal peaks of SO_4^{2-} are generally in line with the observations, but few distinct sub-daily peaks are missed (*e.g.*, on the 6th, 8th and 10th of July, see Fig. 6). The modeled ammonium (NH_4^+) is in line with the observed one (Obs: 0.46 ± 0.22 μg m^{-3}; Mod: 0.47 ± 0.37 μg m^{-3}), with the exception of the 16th and 17th, when all inorganic species are overestimated in the model (the period coincides with large-scale northerly flow from continental Europe). By contrast, the nitrate (NO_3^-) mean concentration was found to be over-predicted (0.56 ± 0.46 μg m^{-3} *versus* 0.30 ± 0.36 μg m^{-3}, modeled and observed values, respectively), mainly due to the 15th–19th period, although the absolute mass concentration was relatively low.

The modeled average organic aerosol (OA) mass concentration was underestimated by about 40% (2.52 ± 1.64 μg m^{-3} *versus* 4.00 ± 2.37 μg m^{-3}, modeled and observed values, respectively) with a moderate correlation coefficient of 0.47, and with better agreement (*i.e.* a less negative bias of 25%) found for the central part of the month (9th–23rd), when most of the observed diurnal maxima are correctly reproduced in the simulation (see Fig. 6) and the correlation coefficient increased to 0.54.

Both major PM_1 components (*e.g.*, OA and sulfate) are within the concentration and relative contribution ranges reported in previous campaigns conducted at CMN[58] as well as at other European background sites, such as Jungfraujoch (2580 m a.s.l., Western Swiss Alps;[23]) and Puy-de-Dome (1465 m a.s.l., central France;[24]).

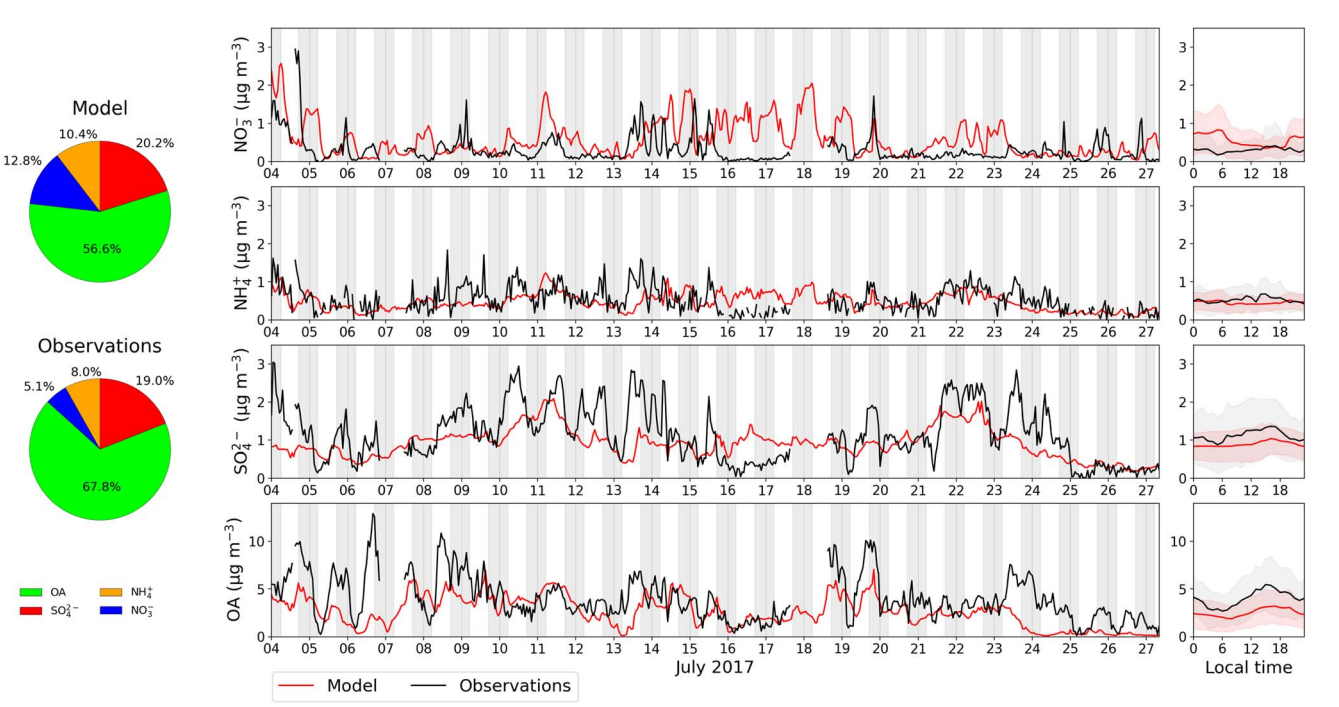

Fig. 6 Pie charts, (left), timeseries (centre) and diurnal cycles (right) of the observed (black) and modeled (red) PM_1 chemical components (NO_3^-, NH_4^+, SO_4^{2-}, OA) during the investigated period (4th–27th July 2017). Centre and right panels share the *y* axis (different between inorganic and organic components). Shaded areas represent nights.

5 Aerosol chemical and regional sources

Aerosol concentrations at CMN analysed in the previous section likely vary because of two superimposed patterns (on top of chemical processes), *i.e.* long-range transport and transport driven by local thermally driven flows. Despite the importance of the former factor, which determines important concentration fluctuations on a weekly scale, we focus here on the latter (*i.e.*, local scale transport) and in particular on the analysis of its typical spatial and temporal evolution on the high resolution domain (d4), which benefits from the meteorological evaluation presented in Section 4.2. In particular, We focus on the OA mass fractions, as they contribute to the majority of the total PM_1 mass at CMN during the investigated period.

As expected, thermally driven flows are typically stronger during anticyclonic and clear sky conditions, corresponding to synoptic phases 1, 3, 4, 6 of the investigated period (see ESI Fig. A1†). In the time gaps between those phases, strong winds impact the Apennines crest either from southwest or from north, and even though thermal breezes can develop to some extent over the lowlands, those days are not considered in this analysis. An exemplary recurrent pattern in most of the investigated days showing well-developed and clearly identifiable thermally-driven flows is represented by the 4th–7th of July. Fig. 7 represents the corresponding average modeled spatial pattern of the wind field during nighttime (5:00 LT) and daytime (15:00 LT; ESI Fig. B2† is analogous for the period 18th–20th). Top panels show the streamlines based on the wind at 10 m a.g.l. for the d4 domain, while the bottom panels report the vertical profiles of potential temperature and horizontal wind speed extracted from a section that extends from the Ligurian Sea to the Po valley (the location of this section is represented as a red line in the top panels). At nighttime (represented by left-hand panels in Fig. 7) ubiquitous katabatic winds cover the Apennines slopes, with stronger intensity on the north-eastern slopes, likely due to the prevalent south-westerly synoptic flow plunging downwind of the ridge at night. Moreover, the coastal regions (southwestern part of the domain) are affected by a weak land breeze directed towards the sea. During the day, sea-to-land and plain-to-mountain circulations develop over most of the d4 domain within some hundreds of metres from the surface, causing advection from the southwestern and northeastern boundaries (corresponding to the Ligurian Sea and the Po valley) towards the Apennines range at the centre of the domain. The proximity of the southwestern slopes to the Ligurian Sea determines an asymmetrical strength of the winds on the southwestern side compared to the ones from the Po valley (northeastern side), as the former are sustained by the see-breeze component. Indeed, where mountain obstacles are lower, the southwesterly flow is able to overstep the ridge and intrude into the Po Plain, especially when thermally driven flows are fully developed (*i.e.*, at 15:00). This is consistent with the model-observations comparison at the station of Vergato (v5), discussed in Section 4.2.2. In contrast, in the model the Po Plain slopes "sheltered" by the ridge extending a few tens of km

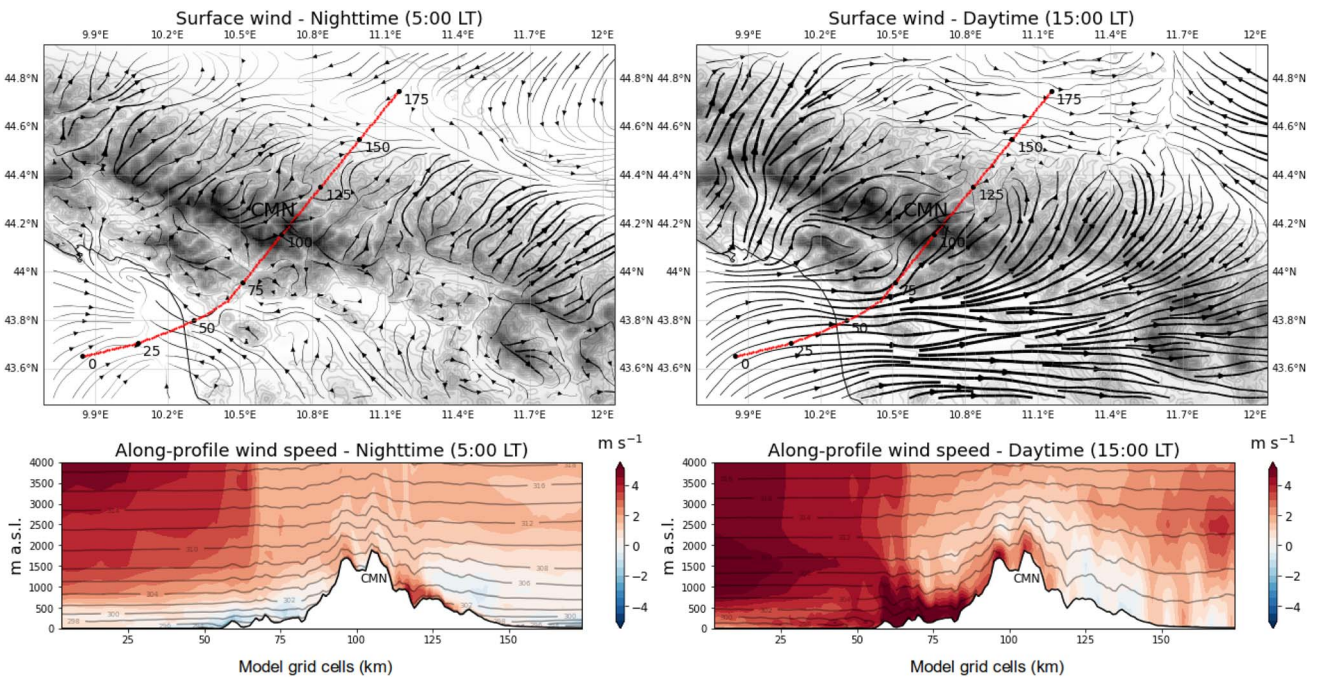

Fig. 7 Top panels: surface streamlines computed from the 10 m-wind over domain d4 (1 km grid-spacing, grey shadowing represents the model topography); bottom panels: vertical distribution of potential temperature and along-profile wind speed; average at 05:00 LT (left) and 13:00 LT (right) for the period 4th–7th July. The location of the vertical section is shown in the top panels as a red line. The numbers on the section represent model grid cells included. Positive values for the along-valley wind refer to west to east winds. An analogous analysis for the period 18th–20th July 2017 is shown in ESI Fig. B2.†

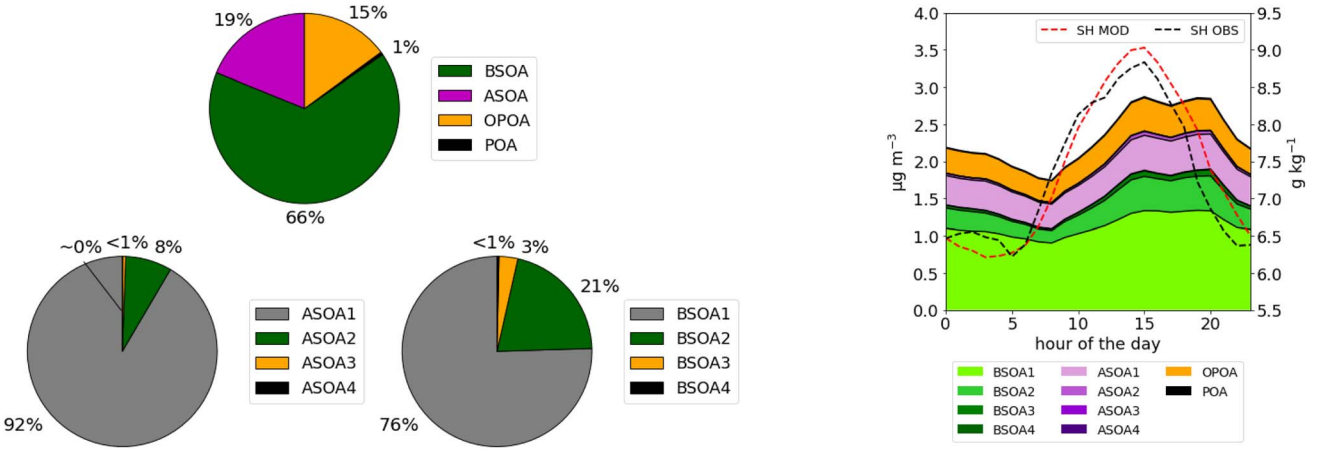

Fig. 8 Composition of the modeled organic aerosol at CMN during the study period. Biogenic secondary organic aerosol (BSOA), anthropogenic secondary organic aerosol (ASOA), oxygenated primary organic aerosol (OPOA, from SVOCs gas-phase oxidation), and primary organic aerosol (POA). ASOA1 to ASOA4, and BSOA1 to BSOA4 indicate the relative contribution of different classes of volatilities to the total ASOA and BSOA (from less volatile, ASOA1 and BSOA1, to more volatile, ASOA4 and BSOA4). On the right, mean diurnal pattern at CMN of organic aerosol (BSOA, ASOA, OPOA, POA) and specific umidity (SH), a tracer for PBL air.

northeast of CMN exhibit more undisturbed up-valley flows from the Po valley, even if less intense than the ones reaching the ridge from the Ligurian Sea. A further perspective on surface flows is provided by the vertical profiles (Fig. 7, bottom panels): during daytime, potential temperature contours (*i.e.* the isentropes) bend down and cross the surface on the southwestern slope especially close to the coast, producing a horizontal pressure gradient leading to surface in-land and up-valley advection (dark red areas), while light blue on the northeastern side indicates less intense wind with opposite direction. Also plain-to-mountain flows generally develop on the southwestern side more slowly than the ones on the northeastern

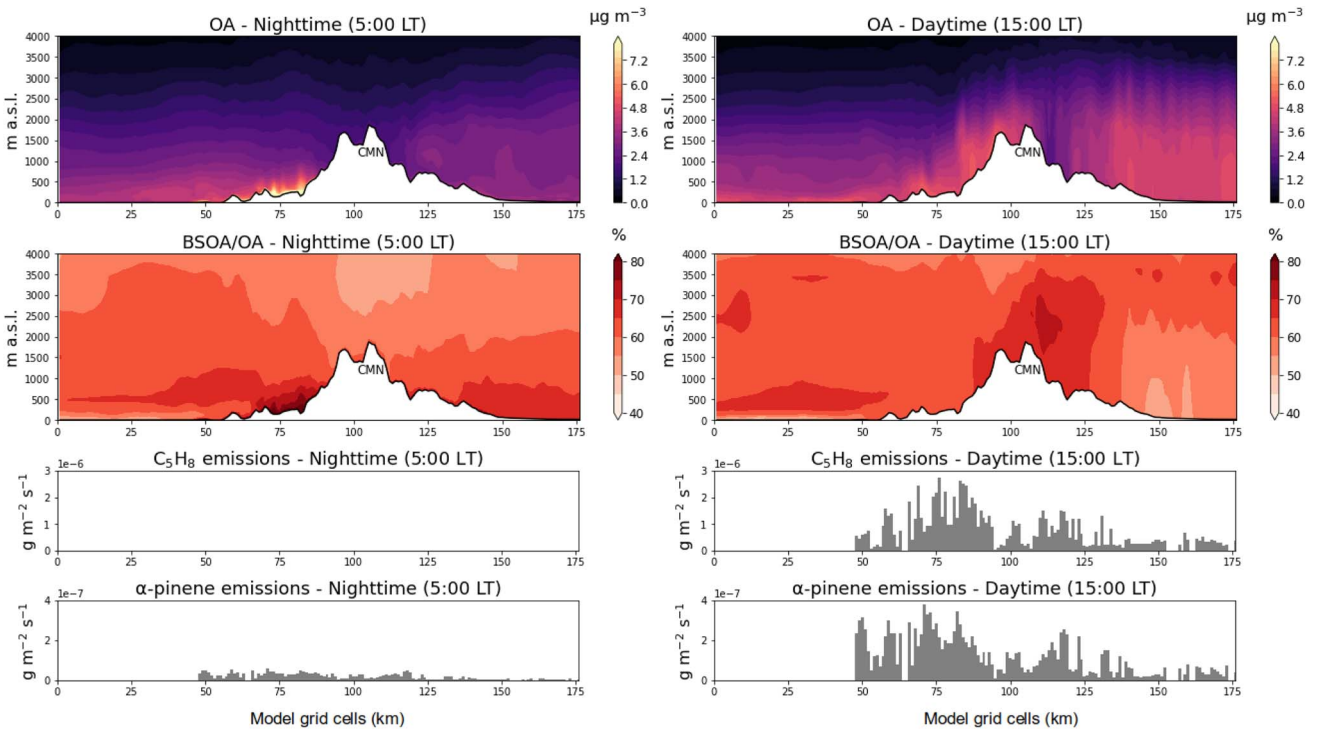

Fig. 9 Top panels: vertical distribution of organic aerosol (OA) mass. Second-row panels: fraction of the biogenic secondary organic aerosol (BSOA) mass over the total OA mass. Third-row panels: emissions of isoprene(C_5H_8). Fourth-row panels: emissions of α-pinene. Average at 5:00 LT (left) and 13:00 LT (right) for the period 4th–7th July. The location of the vertical section is shown in Fig. 7 as a red line. An analogous analysis for the period 18th–20th July 2017 is shown in ESI Fig. B3.†

side, which are already present at mid-morning and are progressively overcome by the opposite component.

Organic aerosol accounts for the largest mass fraction (56.6%) of the total PM_1 modeled at CMN during the investigated period (Section 4.3) with about two-thirds of the OA mass (about 66%) being of biogenic origin (Fig. 8). We investigated the contribution of different classes of volatilities to the total ASOA and BSOA concentrations (Fig. 8). ASOA was almost completely dominated by the low-volatility organic class (ASOA1, at $C^* = 1$ μg m^{-3}) underling the influence of very highly oxygenated air masses typically related to long-range transportation processes. BSOA, however, shows higher contribution from more volatile organic compounds in the $C^* = 10$ μg m^{-3} range (*i.e.*, BSOA2), revealing an additional influence of local emissions and formation processes to BSOA in the surrounding areas of CMN, *i.e.* the Apennines range. High biogenic emissions in the simulation were estimated over most of the Apennines valleys surrounding CMN, while the surrounding plain areas over domain d4 were characterised by less intense biogenic activity (see ESI Fig. B5†). Fig. 9 (top panels) reports the evolution of the vertical distribution of organic aerosol particles during nighttime and daytime and the contribution of biogenic OA to the total OA (along the investigated profile) for the period 4th–7th July. During nighttime, valley floors show high OA concentrations, with peaks of 8 μg m^{-3} possibly resulting from accumulation driven by katabatic winds, and weak dispersion. On the other hand, over the northeastern slope stronger nocturnal surface winds might determine a stronger ventilation of the valley atmospheres and, consequently, lower aerosol concentrations (see Fig. 9). The top right panel in Fig. 9 indicates that the ridge is influenced by high concentrations around 15:00–16:00 LT, likely as a consequence of transportation and formation processes of biogenic aerosols mostly from the southwestern valleys. On the northeastern side (facing the Po valley), OA concentrations reached a maximum of about 5 μg m^{-3} at about 2000 m from the ground, with a relevant fraction of it being of anthropogenic origin over the Po Valley plain. Fig. 9 also shows the distribution of biogenic organic precursors of OA, *i.e.* isoprene and α-pinene, which are emitted mostly in the valleys to the southwest of the Apennines range, and show a minimum at the highest elevations.

It is plausible that the underestimation of the OA fraction and the overestimation of the nitrate fraction at CMN in the simulation (Fig. 6 and Table 2) might be triggered by an underestimation of biogenic volatile organic compounds (BVOCs), which might shift the atmospheric oxidations towards inorganic gas-phase compounds, therefore enhancing the production of inorganic aerosols such as nitrates. CTM intercomparison projects have reported similar model performance, *i.e.*, overprediction of nitrate and underprediction of the OA fraction.[59,60] Moreover, two recent model applications, both performed with the MEGAN 2.1 emission model during summer periods in Europe indicated an underprediction of monoterpenes air concentrations, which might point towards an underestimation of their emissions.[48,61]

Table 2 Root Mean Square Error (RMSE), Mean Bias Error (MBE) and correlation coefficient (*R*) calculated as in Section 3.2.2 for PM_1 components at CMN during the study period. Units for RMSE, MBE, Mean and SD are μg m^{-3}

Species	RMSE	MBE	R	Mean model	Mean observations	SD model	SD observations
NO_3^-	0.58	0.25	0.18	0.56	0.30	0.46	0.36
NH_4^+	0.37	−0.02	0.30	0.47	0.46	0.37	0.22
SO_4^{2-}	0.63	−0.22	0.59	0.89	1.12	0.39	0.73
OA	2.62	−1.48	0.47	2.52	4.00	1.64	2.37

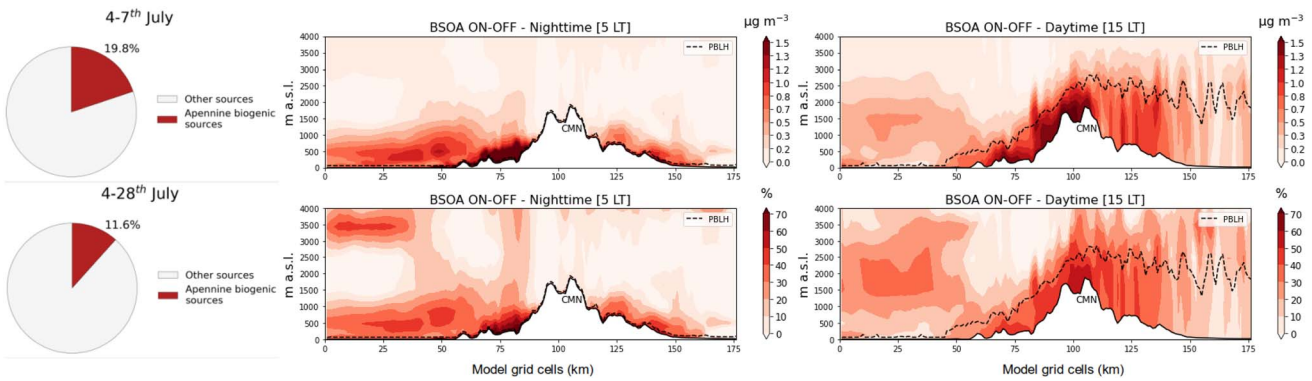

Fig. 10 Pie charts reporting the impact of biogenic emissions from the Apennines on total OA concentrations for the 4th–7th July and for the whole period (left-hand plots). Absolute (right-hand top panels) and relative (right-hand bottom panels) difference in BSOA concentration between the base case (with biogenic emissions, "ON") and the sensitivity simulation (without biogenic emissions, "OFF") and PBL height in the base case (dashed line). Average at 5:00 LT (left) and 13:00 LT (right) for the period 4th–7th July. The location of the vertical section is shown in Fig. 7 as a red line. An analogous analysis for the period 18th–20th July 2017 is shown in ESI Fig. B3.†

Finally, we performed an additional model run by inhibiting (zeroing) biogenic emissions over the Apennines range in domain d4 (*i.e.* only over the mountains). Fig. 10 reports the absolute and relative difference in BSOA concentrations between the simulation with ("ON") and without ("OFF") biogenic emissions over the northern Apennines. The plots show that during nocturnal hours (5:00 LT) differences, *i.e.* reductions, in BSOA concentration are up to 70% (5 μg m^{-3}) close to the surface on the southwest of CMN and up to 50% (2 μg m^{-3}) over the northeastern slopes. At 15:00 LT, the differences are about 60% (2 μg m^{-3}) on the southwestern slope, which is affected by the transport by thermally driven winds, with a peak of 70% (1.8 μg m^{-3}) found in proximity of CMN. Interestingly, the impact of biogenic local emissions, allocated only at the surface layer of the model, is visible in a depth of about 1.5 km above the southwestern Apennines slope, extending horizontally and above the PBL height over the northeastern slope. This pattern might suggest that biogenic OA originating in valleys located in the southwestern part of the domain can be transported towards high altitudes by valley winds and can eventually impact the aerosol load in the free troposphere.

6 Conclusions

We presented a chemical transport model application covering the month of July in 2017 with a focus over the northern Apennines, specifically over the area of the WMO/GAW station of Mt. Cimone. The model was set-up in a high resolution configuration (1 km) to represent the typical summertime wind patterns developing at the interface between the plains, valleys and ridges of the northern Apennines mountains. Model results were evaluated against meteorological and aerosol observational data. In particular, we focused on the near-surface meteorological dynamics over complex terrain, on the aerosol composition at Mt. Cimone and on the aerosol sources and transport mechanisms from the lowlands towards the Apennines ridge.

On the basis of the meteorological evaluation, various conclusions can be drawn. In the plain and in the valleys to the southwest of CMN the modeled winds fields are well reproduced, both in terms of timing and intensity. A less clear pattern is found on the northeastern slope, with indications that the model could be underestimating the thermally-driven mountain circulations in the valleys north of CMN. On the ridges the wind dynamics are generally well captured on a day-to-day scale in the model. However, the approximated model topography is believed to cause a mismatch in the diurnal variation of the modeled wind speed which could affect the vertical exchanges between the valley atmosphere and the mountain top. This is more evident at the WMO/GAW station of Mt. Cimone than at other ridge sites.

The measuring site of CMN might be particularly affected by local effects induced by the morphology of the mountain top which are not reproduced at the resolution of the simulation. For example, a coherent pattern of high wind speeds associated with a specific wind direction found among all the ridge stations is modeled but not observed at CMN. Looking ahead, a practical approach to further investigate the last two points without increasing the resolution of the model is the straightforward "manual" correction of the local terrain height in the surroundings of CMN, in order to test the sensitivity of the modeled wind speed to the model topography. However, such manual terrain model modifications of the domain should be cautiously applied in order not to compromise the numerical stability. Moreover, the effect of physical processes occurring at or below the "grey zone" (*i.e.*, below the 1 km scale), such as most of the turbulence parameterizations, crucial in pollutant dispersion, should be carefully taken into account. The results presented here suggest that a future deployment of an additional anemometer located on the highest point of Mt. Cimone (despite challenging wind conditions), and a follow-up intercomparison with the anemometers currently installed at CMN, might greatly help in elucidating the level of representativeness of the anemometers currently in operation at CMN. Finally, despite the local complex characteristics of the analyzed area, the meteorological model configuration provided an accurate representation of sea and mountain breezes, as shown also in similar studies performed in other complex terrain areas.[10,53] This configuration may be applied to further case studies or to a longer period over the same domain, in order to have a comprehensive characterization of summer meteorological patterns at CMN.

WRF-CHIMERE could reasonably reproduce the relative abundance and temporal variation of the main chemical components of PM_1 observed at CMN. The major components were organic and sulphate aerosols, constituting 57% and 20% of the PM_1 mass at CMN in the model simulation during the investigated period. Most of the OA modeled at CMN was of biogenic origin (66%) which was, however, predicted to be less oxidized compared to its anthropogenic fraction, underlying the additional importance of the local biogenic emissions located in the Apennines. Therefore, a shorter subset of days prone to the full development of thermally-driven winds were selected in order to investigate their role in transporting aerosol particles from the Apennines valleys. At their fully developed stage, *i.e.* around 15:00–16:00 LT, coastal and mountain-induced winds are directed from the sea and from the lowlands towards the Apennines range, with a stronger component over the southwestern slopes, consistent with the meteorological evaluation. Our model simulations indicate that organic aerosols at CMN are likely affected by such local-scale process (on top of long-range transport processes), initiated by the emission of biogenic gaseous precursors in the Apennines valleys and followed by their chemical conversion to OA during their day-time up-valley transport, ultimately altering the aerosol concentrations above the predicted PBL height. These results align with previous research[10,53] and imply that mountain regions might being injecting currently unknow quantities of biogenic particles in the upper layer of the atmosphere, with unknown consequences on the Earths' climate. Since such mechanism is not currently included in current future climate calculations due to the coarse resolution of climate models (which are not able to resolve valley winds), more research is needed to

properly quantify, and parameterize, mountain effects on aerosol concentrations.

Results from the present study will be beneficial to a series of applications over complex terrain[62] and further insight on these processes are expected from the forthcoming field campaigns foreseen within the international cooperation project TEAMx.[63,64]

Data availability

The CHIMERE air quality model is available from **https://www.lmd.polytechnique.fr/chimere/** (registration required). The model and observational data can be obtained upon request from the corresponding authors.

Author contributions

GC designed the study. BV wrote and developed the code used for the analysis, prepared the model input data, and run all the model simulations. AC provided extensive support in running the WRF-CHIMERE model and with the preparation of model data. MB, AC, DZ, JM, VS, PC, AM, MM, LH, MA, MP, BB, PT, FB participated in data collection and/or discussion of the analysis. BV and GC prepared the first version of the manuscript with contributions from all co-authors. All authors approved the final version of the paper.

Conflicts of interest

The contact author has declared that none of the authors has any competing interests.

Acknowledgements

This work was supported by the European Research Council *via* the project CHAPAs (No. 850614), the Jenny and Antti Wihuri Foundation (220036) and by the Academy of Finland (No. 311932, 307537, 334792, 337549). Model simulations were performed "online" with the meteorological model on the mahti supercomputer of the Finnish IT center for science (project 2005956). We would like to thank Juha Lento for his continuous support at the Finnish IT center for science (CSC). We acknowledge the EC funded project ACTRIS-2 (grant agreement no.: 654109; now integrated in ACTRIS ERIC) for the 2017 Po Valley experiment support and for providing support to A. Minna to access Monte Cimone station. We further thank the Consiglio Nazionale delle Ricerche (CNR) and the Centro Aeronautica Militare di Montagna (CAMM) for the support in data collection. CNR-ISAC acknowledge the support of the Italian Ministry for Universities and Research (MIUR/MUR) by the Joint Research Unit ICOS-Italy.

References

1 P. L. Jackson, G. Mayr and S. Vosper, in *Dynamically-Driven Winds*, ed. F. K. Chow, S. F. J. De Wekker and B. J. Snyder, Springer Netherlands, Dordrecht, 2013, pp. 121–218.

2 D. Zardi and C. D. Whiteman, in *Diurnal Mountain Wind Systems*, ed. F. K. Chow, S. F. J. De Wekker and B. J. Snyder, Springer Netherlands, Dordrecht, 2013, pp. 35–119. Available from, DOI: **10.1007/978-94-007-4098-3_2**.

3 R. Urgnani, A. Finco, M. Chiesa, R. Marzuoli, L. Bignotti, A. Riccio, *et al.*, Size-segregated aerosol fluxes, deposition velocities, and chemical composition in an Alpine valley, *Atmos. Res.*, 2022, **268**, 105995. Available from: **https://www.sciencedirect.com/science/article/pii/S0169809521005512**.

4 M. W. Rotach and D. Zardi, On the boundary-layer structure over highly complex terrain: Key findings from MAP, *Q. J. R. Metereol. Soc.*, 2007, **133**(625), 937–948.

5 D. G. Steyn, S. F. J. De Wekker, M. Kossmann and A. Martilli, in *Boundary Layers and Air Quality in Mountainous Terrain*, ed. F. K. Chow, S. F. J. De Wekker and B. J. Snyder, Springer Netherlands, Dordrecht, 2013. pp. 261–289.

6 D. Zardi and M. W. Rotach, Transport and Exchange Processes in the Atmosphere over Mountainous Terrain: Perspectives and Challenges for Observational and Modelling Systems, from Local to Climate Scales, *Atmosphere*, 2021, **12**(2), 199. Available from: **https://www.mdpi.com/2073-4433/12/2/199**.

7 L. Giovannini, E. Ferrero, T. Karl, M. W. Rotach, C. Staquet, S. Trini Castelli, *et al.*, Atmospheric Pollutant Dispersion over Complex Terrain: Challenges and Needs for Improving Air Quality Measurements and Modeling, *Atmosphere*, 2020, **11**(6), 646. Available from: **https://www.mdpi.com/2073-4433/11/6/646**.

8 J. Schmidli, S. Böing and O. Fuhrer, Accuracy of Simulated Diurnal Valley Winds in the Swiss Alps: Influence of Grid Resolution, Topography Filtering, and Land Surface Datasets, *Atmosphere*, 2018, **9**(5), 196. Available from: **https://www.mdpi.com/2073-4433/9/5/196**.

9 J. S. Wagner, A. Gohm and M. W. Rotach, The Impact of Horizontal Model Grid Resolution on the Boundary Layer Structure over an Idealized Valley, *Mon. Weather Rev.*, 2014, **142**(9), 3446–3465. Available from: **https://journals.ametsoc.org/view/journals/mwre/142/9/mwr-d-14-00002.1.xml**.

10 J. Mikkola, V. A. Sinclair, M. Bister and F. Bianchi, Daytime along-valley winds in the Himalayas as simulated by the Weather Research and Forecasting (WRF) model, *Atmos. Chem. Phys.*, 2023, **23**(2), 821–842. Available from: **https://acp.copernicus.org/articles/23/821/2023/**.

11 G. Ciarelli, J. Jiang, I. El Haddad, A. Bigi, S. Aksoyoglu, A. S. H. Prévôt, *et al.*, Modeling the effect of reduced traffic due to COVID-19 measures on air quality using a chemical transport model: impacts on the Po Valley and the Swiss Plateau regions, *Environ. Sci.: Atmos.*, 2021, **1**, 228–240, DOI: **10.1039/D1EA00036E**.

12 G. Pirovano, C. Colombi, A. Balzarini, G. M. Riva, V. Gianelle and G. Lonati, PM2.5 source apportionment in Lombardy (Italy): Comparison of receptor and chemistry-transport modelling results, *Atmos. Environ.*, 2015, **106**, 56–70. Available from: **https://www.sciencedirect.com/science/article/pii/S1352231015000965**.

13 A. Meroni, G. Pirovano, S. Gilardoni, G. Lonati, C. Colombi, V. Gianelle, *et al.*, Investigating the role of chemical and physical processes on organic aerosol modelling with CAMx in the Po Valley during a winter episode, *Atmos. Environ.*, 2017, **171**, 126–142. Available from: https://www.sciencedirect.com/science/article/pii/S1352231017306659.

14 G. Veratti, A. Bigi, A. Lupascu, T. M. Butler and G. Ghermandi, Urban population exposure forecast system to predict NO_2 impact by a building-resolving multi-scale model approach, *Atmos. Environ.*, 2021, **261**, 118566. Available from: https://www.sciencedirect.com/science/article/pii/S1352231021003885.

15 N. Pepe, G. Pirovano, A. Balzarini, A. Toppetti, G. M. Riva, F. Amato, *et al.*, Enhanced CAMx source apportionment analysis at an urban receptor in Milan based on source categories and emission regions, *Atmos. Environ.: X*, 2019, **2**, 100020. Available from: https://www.sciencedirect.com/science/article/pii/S2590162119300231.

16 D. Zardi, M. Falocchi, L. Giovannini, W. Tirler, E. Tomasi, G. Antonacci, *et al.*, The Bolzano Tracer Experiment (BTEX), *Bull. Am. Meteorol. Soc.*, 2021, **102**(5), E966–E989.

17 M. Falocchi, D. Zardi and L. Giovannini, Meteorological normalization of NO_2 concentrations in the Province of Bolzano (Italian Alps), *Atmos. Environ.*, 2021, **246**, 118048. Available from: https://www.sciencedirect.com/science/article/pii/S1352231020307809.

18 M. Falocchi, L. Giovannini, M. de Franceschi and D. Zardi, A method to determine the characteristic time-scales of quasi-isotropic surface-layer turbulence over complex terrain: A case-study in the Adige Valley (Italian Alps), *Q. J. R. Metereol. Soc.*, 2019, **145**(719), 495–512.

19 M. Falocchi, W. Tirler, L. Giovannini, E. Tomasi, G. Antonacci and D. Zardi, A dataset of tracer concentrations and meteorological observations from the Bolzano Tracer EXperiment (BTEX) to characterize pollutant dispersion processes in an Alpine valley, *Earth Syst. Sci. Data*, 2020, **12**(1), 277–291. Available from: https://essd.copernicus.org/articles/12/277/2020/.

20 E. Tomasi, L. Giovannini, D. Zardi and M. de Franceschi, Optimization of Noah and Noah-MP WRF Land Surface Schemes in Snow-Melting Conditions over Complex Terrain, *Mon. Weather Rev.*, 2017, **145**(12), 4727–4745.

21 E. Tomasi, L. Giovannini, M. Falocchi, G. Antonacci, P. A. Jiménez, B. Kosovic, *et al.*, Turbulence parameterizations for dispersion in sub-kilometer horizontally non-homogeneous flows, *Atmos. Res.*, 2019, **228**, 122–136. Available from: https://www.sciencedirect.com/science/article/pii/S0169809518316387.

22 H. Diémoz, F. Barnaba, T. Magri, G. Pession, D. Dionisi, S. Pittavino, *et al.*, Transport of Po Valley aerosol pollution to the northwestern Alps – Part 1: Phenomenology, *Atmos. Chem. Phys.*, 2019, **19**(5), 3065–3095. Available from: https://acp.copernicus.org/articles/19/3065/2019/.

23 J. Cozic, B. Verheggen, E. Weingartner, J. Crosier, K. N. Bower, M. Flynn, *et al.*, Chemical composition of free tropospheric aerosol for PM1 and coarse mode at the high alpine site Jungfraujoch, *Atmos. Chem. Phys.*, 2008, **8**(2), 407–423. Available from: https://acp.copernicus.org/articles/8/407/2008/.

24 E. J. Freney, K. Sellegri, F. Canonaco, J. Boulon, M. Hervo, R. Weigel, *et al.*, Seasonal variations in aerosol particle composition at the puy-de-Dôme research station in France, *Atmos. Chem. Phys.*, 2011, **11**(24), 13047–13059. Available from: https://acp.copernicus.org/articles/11/13047/2011/.

25 P. Cristofanelli, E. Brattich, S. Decesari, T. Landi, M. Maione, D. Putero, *et al.*, in *The "O. Vittori" Observatory at Mt. Cimone: A "Lighthouse" for the Mediterranean Troposphere*, 2018, pp. 1–14.

26 E. Brattich, H. Liu, L. Tositti, D. B. Considine and J. H. Crawford, Processes controlling the seasonal variations in ^{210}Pb and ^{7}Be at the Mt. Cimone WMO-GAW global station, Italy: a model analysis, *Atmos. Chem. Phys.*, 2017, **17**(2), 1061–1080. Available from: https://acp.copernicus.org/articles/17/1061/2017/.

27 L. Menut, B. Bessagnet, R. Briant, A. Cholakian, F. Couvidat, S. Mailler, *et al.*, The CHIMERE v2020r1 online chemistry-transport model, *Geosci. Model Dev.*, 2021, **14**(11), 6781–6811. Available from: https://gmd.copernicus.org/articles/14/6781/2021/.

28 P. Cristofanelli, I. Gutiérrez, J. A. Adame, P. Bonasoni, M. Busetto, F. Calzolari, *et al.*, Interannual and seasonal variability of NO_x observed at the Mt. Cimone GAW/WMO global station (2165 m a.s.l., Italy), *Atmos. Environ.*, 2021, **249**, 118245. Available from: https://www.sciencedirect.com/science/article/pii/S1352231021000637.

29 N. L. Ng, S. C. Herndon, A. Trimborn, M. R. Canagaratna, P. L. Croteau, T. B. Onasch, D. Sueper, D. R. Worsnop, *et al.*, An Aerosol Chemical Speciation Monitor (ACSM) for Routine Monitoring of the Composition and Mass Concentrations of Ambient Aerosol, *Aerosol Sci. Technol.*, 2011, **45**(7), 780–794, DOI: 10.1080/02786826.2011.560211.

30 B. Bessagnet, G. Pirovano, M. Mircea, C. Cuvelier, A. Aulinger, G. Calori, *et al.*, Presentation of the EURODELTA III intercomparison exercise – evaluation of the chemistry transport models' performance on criteria pollutants and joint analysis with meteorology, *Atmos. Chem. Phys.*, 2016, **16**(19), 12667–12701. Available from: https://acp.copernicus.org/articles/16/12667/2016/.

31 G. Ciarelli, M. R. Theobald, M. G. Vivanco, M. Beekmann, W. Aas, C. Andersson, *et al.*, Trends of inorganic and organic aerosols and precursor gases in Europe: insights from the EURODELTA multi-model experiment over the 1990–2010 period, *Geosci. Model Dev.*, 2019, **12**(12), 4923–4954. Available from: https://gmd.copernicus.org/articles/12/4923/2019/.

32 L. Fink, M. Karl, V. Matthias, S. Oppo, R. Kranenburg, J. Kuenen, *et al.*, A multimodel evaluation of the potential impact of shipping on particle species in the Mediterranean Sea, *Atmos. Chem. Phys.*, 2023, **23**, 10163–

10189. Available from: https://egusphere.copernicus.org/preprints/2023/egusphere-2023-406/.

33 S. Galmarini, B. Koffi, E. Solazzo, T. Keating, C. Hogrefe, M. Schulz, *et al.*, Technical note: Coordination and harmonization of the multi-scale, multi-model activities HTAP2, AQMEII3, and MICS-Asia3: simulations, emission inventories, boundary conditions, and model output formats, *Atmos. Chem. Phys.*, 2017, **17**(2), 1543–1555. Available from: https://acp.copernicus.org/articles/17/1543/2017/.

34 G. Pirovano, A. Balzarini, B. Bessagnet, C. Emery, G. Kallos, F. Meleux, *et al.*, Investigating impacts of chemistry and transport model formulation on model performance at European scale, *Atmos. Environ.*, 2012, **53**, 93–109.

35 E. Solazzo, C. Hogrefe, A. Colette, M. Garcia-Vivanco and S. Galmarini, Advanced error diagnostics of the CMAQ and Chimere modelling systems within the AQMEII3 model evaluation framework, *Atmos. Chem. Phys.*, 2017, **17**(17), 10435–10465. Available from: https://acp.copernicus.org/articles/17/10435/2017/.

36 M. R. Theobald, M. G. Vivanco, W. Aas, C. Andersson, G. Ciarelli, F. Couvidat, *et al.*, An evaluation of European nitrogen and sulfur wet deposition and their trends estimated by six chemistry transport models for the period 1990–2010, *Atmos. Chem. Phys.*, 2019, **19**(1), 379–405. Available from: https://acp.copernicus.org/articles/19/379/2019/.

37 S. Tsyro, W. Aas, A. Colette, C. Andersson, B. Bessagnet, G. Ciarelli, *et al.*, Eurodelta multi-model simulated and observed particulate matter trends in Europe in the period of 1990–2010, *Atmos. Chem. Phys.*, 2022, **22**(11), 7207–7257. Available from: https://acp.copernicus.org/articles/22/7207/2022/.

38 C. Gao, X. Zhang, A. Xiu, Q. Tong, H. Zhao, S. Zhang, *et al.*, Intercomparison of multiple two-way coupled meteorology and air quality models (WRF v4.1.1–CMAQ v5.3.1, WRF–Chem v4.1.1, and WRF v3.7.1–CHIMERE v2020r1) in eastern China, *Geosci. Model Dev.*, 2024, **17**(6), 2471–2492. Available from: https://gmd.copernicus.org/articles/17/2471/2024/.

39 C. Derognat, M. Beekmann, M. Baeumle, D. Martin and H. Schmidt, Effect of biogenic volatile organic compound emissions on tropospheric chemistry during the Atmospheric Pollution Over the Paris Area (ESQUIF) campaign in the Ile-de-France region, *J. Geophys. Res.: Atmos.*, 2003, **108**(D17), 8560. Available from: https://agupubs.onlinelibrary.wiley.com/doi/abs/10.1029/2001JD001421.

40 W. Carter, Documentation of the SAPRC-99 Chemical Mechanism for VOC Reactivity Assessment, *Final Report to California Air Resources Board*, 2000.

41 A. Nenes, S. Pandis and C. Pilinis, ISORROPIA: A New Thermodynamic Equilibrium Model for Multiphase Multicomponent Inorganic Aerosols, *Aquat. Geochem.*, 1998, **4**, 123–152.

42 E. Debry, K. Fahey, K. Sartelet, B. Sportisse and M. Tombette, Technical note: A new SIze REsolved aerosol model (SIREAM), *Atmos. Chem. Phys.*, 2007, **7**, 1537–1547, DOI: 10.5194/acp-7-1537-2007.

43 M. Kulmala, A. Laaksonen and L. Pirjola, Parameterizations for sulfuric acid/water nucleation rates, *J. Geophys. Res.: Atmos.*, 1998, **103**(D7), 8301–8307. Available from: https://agupubs.onlinelibrary.wiley.com/doi/abs/10.1029/97JD03718.

44 Q. J. Zhang, M. Beekmann, F. Drewnick, F. Freutel, J. Schneider, M. Crippa, *et al.*, Formation of organic aerosol in the Paris region during the MEGAPOLI summer campaign: evaluation of the volatility-basis-set approach within the CHIMERE model, *Atmos. Chem. Phys.*, 2013, **13**(11), 5767–5790. Available from: https://acp.copernicus.org/articles/13/5767/2013/.

45 A. Cholakian, M. Beekmann, A. Colette, I. Coll, G. Siour, J. Sciare, *et al.*, Simulation of fine organic aerosols in the western Mediterranean area during the ChArMEx 2013 summer campaign, *Atmos. Chem. Phys.*, 2018, **18**(10), 7287–7312. Available from: https://acp.copernicus.org/articles/18/7287/2018/.

46 B. N. Murphy and S. N. Pandis, Simulating the Formation of Semivolatile Primary and Secondary Organic Aerosol in a Regional Chemical Transport Model, *Environ. Sci. Technol.*, 2009, **43**(13), 4722–4728, DOI: 10.1021/es803168a.

47 R. Bergström, H. A. C. Denier van der Gon, A. S. H. Prévôt, K. E. Yttri and D. Simpson, Modelling of organic aerosols over Europe (2002–2007) using a volatility basis set (VBS) framework: application of different assumptions regarding the formation of secondary organic aerosol, *Atmos. Chem. Phys.*, 2012, **12**(18), 8499–8527. Available from: https://acp.copernicus.org/articles/12/8499/2012/.

48 G. Ciarelli, S. Tahvonen, A. Cholakian, M. Bettineschi, B. Vitali, T. Petäjä, *et al.*, On the formation of biogenic secondary organic aerosol in chemical transport models: an evaluation of the WRF-CHIMERE (v2020r2) model with a focus over the Finnish boreal forest, *Geosci. Model Dev.*, 2024, **17**(2), 545–565. Available from: https://gmd.copernicus.org/articles/17/545/2024/.

49 W. C. Skamarock, J. Klemp, J. Dudhia, D. O. Gill, D. Barker, W. Wang, *et al.*, *A Description of the Advanced Research WRF Version 3*, 2008 01, 27, pp. 3–27.

50 E. J. Mlawer, S. J. Taubman, P. D. Brown, M. J. Iacono and S. A. Clough, Radiative transfer for inhomogeneous atmospheres: RRTM, a validated correlated-k model for the longwave, *J. Geophys. Res.: Atmos.*, 1997, **102**(D14), 16663–16682. Available from: https://agupubs.onlinelibrary.wiley.com/doi/abs/10.1029/97JD00237.

51 S. Y. Hong, J. Dudhia and S. H. Chen, A Revised Approach to Ice Microphysical Processes for the Bulk Parameterization of Clouds and Precipitation, *Mon. Weather Rev.*, 2004, **132**(1), 103–120. Available from: https://journals.ametsoc.org/view/journals/mwre/132/1/1520-0493_2004_132_0103_aratim_2.0.co_2.xml.

52 F. Chen and J. Dudhia, Coupling an Advanced Land Surface–Hydrology Model with the Penn State–NCAR MM5 Modeling System. Part I: Model Implementation and Sensitivity, *Mon.*

Weather Rev., 2001, **129**(4), 569–585. Available from: https://journals.ametsoc.org/view/journals/mwre/129/4/1520-0493_2001_129_0569_caalsh_2.0.co_2.xml.

53 F. Bianchi, H. Junninen, A. Bigi, V. A. Sinclair, L. Dada, C. R. Hoyle, *et al.*, Biogenic particles formed in the Himalaya as an important source of free tropospheric aerosols, *Nat. Geosci.*, 2020, **14**(1), 4–9.

54 A. B. Guenther, X. Jiang, C. L. Heald, T. Sakulyanontvittaya, T. Duhl, L. K. Emmons, *et al.*, The Model of Emissions of Gases and Aerosols from Nature version 2.1 (MEGAN2.1): an extended and updated framework for modeling biogenic emissions, *Geosci. Model Dev.*, 2012, **5**(6), 1471–1492. Available from: https://gmd.copernicus.org/articles/5/1471/2012/.

55 D. A. Hauglustaine, Y. Balkanski and M. Schulz, A global model simulation of present and future nitrate aerosols and their direct radiative forcing of climate, *Atmos. Chem. Phys.*, 2014, **14**(20), 11031–11063. Available from: https://acp.copernicus.org/articles/14/11031/2014/.

56 M. Chin, P. Ginoux, S. Kinne, O. Torres, B. Holben, B. Duncan, *et al.*, Tropospheric Aerosol Optical Thickness from the GOCART Model and Comparisons with Satellite and Sun Photometer Measurements, *J. Atmos. Sci.*, 2002, **59**, 461–483, DOI: 10.1175/1520-0469(2002)059<0461:TAOTFT>2.0.CO;2.

57 Arpae, *Rapporto IdroMeteoClima 2017*, 2018. Available from: https://www.arpae.it/it/temi-ambientali/meteo/report-meteo/rapporti-annuali/report_idrometeo_web.pdf/view.

58 M. Rinaldi, S. Gilardoni, M. Paglione, S. Sandrini, S. Fuzzi, P. Massoli, *et al.*, Organic aerosol evolution and transport observed at Mt. Cimone (2165 m a.s.l.), Italy, during the PEGASOS campaign, *Atmos. Chem. Phys.*, 2015, **15**(19), 11327–11340. Available from: https://acp.copernicus.org/articles/15/11327/2015/.

59 G. Ciarelli, S. Aksoyoglu, M. Crippa, J. L. Jimenez, E. Nemitz, K. Sellegri, *et al.*, Evaluation of European air quality modelled by CAMx including the volatility basis set scheme, *Atmos. Chem. Phys.*, 2016, **16**(16), 10313–10332. Available from: https://acp.copernicus.org/articles/16/10313/2016/.

60 J. Jiang, S. Aksoyoglu, G. Ciarelli, E. Oikonomakis, I. El-Haddad, F. Canonaco, *et al.*, Effects of two different biogenic emission models on modelled ozone and aerosol concentrations in Europe, *Atmos. Chem. Phys.*, 2019, **19**(6), 3747–3768. Available from: https://acp.copernicus.org/articles/19/3747/2019/.

61 A. Cholakian, M. Beekmann, G. Siour, I. Coll, M. Cirtog, E. Ormeño, *et al.*, Simulation of organic aerosol, its precursors, and related oxidants in the Landes pine forest in southwestern France: accounting for domain-specific land use and physical conditions, *Atmos. Chem. Phys.*, 2023, **23**(6), 3679–3706. Available from: https://acp.copernicus.org/articles/23/3679/2023/.

62 S. F. J. De Wekker, M. Kossmann, J. C. Knievel, L. Giovannini, E. D. Gutmann and D. Zardi, Meteorological Applications Benefiting from an Improved Understanding of Atmospheric Exchange Processes over Mountains, *Atmosphere*, 2018, **9**(10), 371. Available from: https://www.mdpi.com/2073-4433/9/10/371.

63 S. Serafin, B. Adler, J. Cuxart, S. F. J. De Wekker, A. Gohm, B. Grisogono, *et al.*, Exchange Processes in the Atmospheric Boundary Layer Over Mountainous Terrain, *Atmosphere*, 2018, **9**(3), DOI: 10.3390/atmos9030102.

64 M. W. Rotach, S. Serafin, H. C. Ward, M. Arpagaus, I. Colfescu, J. Cuxart, *et al.*, A Collaborative Effort to Better Understand, Measure, and Model Atmospheric Exchange Processes over Mountains, *Bull. Am. Meteorol. Soc.*, 2022, **103**(5), E1282–E1295. Available from: https://journals.ametsoc.org/view/journals/bams/103/5/BAMS-D-21-0232.1.xml.